Unbinding of hACE2 and Inhibitors from the Receptor Binding Domain of SARS-CoV-2 Spike Protein

Lokpati Mishra[1] *and Tusar Bandyopadhyay*[2,]*

[1]Radiation Safety Systems Division, Bhabha Atomic Research Centre, Mumbai 400 085, India.

[2]Theoretical Chemistry Section, Chemistry Division, Bhabha Atomic Research Centre, Mumbai 400 085, India

(*email: btusar@barc.gov.in)

KEYWORDS: *SARS-CoV-2 (Covid 19) spike protein receptor binding domain, mutated antibody, nanobody-derived peptide inhibitor, MD simulations, unbinding transitions*

ABSTRACT: The first direful biomolecular event leading to COVID-19 disease is the SARS-CoV-2 virus surface spike (S) protein-mediated interaction with the human transmembrane protein, angiotensin-converting enzyme 2 (hACE2). Prevention of this interaction presents an attractive alternative to thwart SARS-CoV-2 replications. The development of monoclonal antibodies (mAbs) in the convalescent plasma treatment, nanobody, and designer peptides, which recognizes epitopes that overlap with hACE2 binding sites in the receptor-binding domain (RBD) of S protein (S/RBD) and thereby blocking the infection has been the center stage of therapeutic research. Here we report atomistic and reliable *in silico* structure-energetic features of the S/RBD interactions with hACE2 and its two inhibitors (convalescent mAb, B38, and an alpaca nanobody, Ty1). The discovered potential of mean forces exhibits free energy basin and barriers along the interaction pathways, providing sufficient molecular insights to design a B38 mutant and a Ty1-based peptide with higher binding capacity. While the mutated B38 forms a 60-fold deeper free energy minimum, the designer peptide (Ty1-based) constitutes 38 amino acids and is found to form a 100-fold deeper free energy minimum in the first binding basin than their wild-type variants in complex with S/RBD. Our strategy may help to design more efficacious biologics towards therapeutic intervention against the current raging pandemic.

1. Introduction

Coronaviruses (CoVs) have always posed a threat to human health. However, severe acute respiratory syndrome coronavirus 2 (SARS-CoV-2) causing the COVID-19 disease have resulted in the current pandemic,[1] lasting over more than a year with devastating effects on human life in addition to causing unprecedented societal and economic damages[2] in almost every corner of the world. Of the seven CoVs known to infect humans, four are relatively harmless causing common cold and cough-related respiratory trouble, while the other three, SARS-CoV-1 (outbreak in 2003) MERS-CoV (outbreak in 2012), and the new entrant SARS-CoV-2, are highly pathogenic. For example, there was a total of 8096 confirmed cases and 774 deaths during the SARS-CoV-1 epidemic outbreak.[3] MERS-CoV, on the other hand, had spread across 27 different countries, causing 2494 cases and 858 deaths.[4] In comparison, as of June 11, 2021, globally there have been over 174 million confirmed cases and 3.7 million deaths caused by the SARS-COV-2 pathogen.[5] Although the fatality rate due to COVID-19 is fortunately much lower than those of SARS and MERS, its very high transmissibility[1] ratio has caused an occasional lockdown and strict social measures a "new normal" worldwide ever since its outbreak in 2019.

The SARS-CoV-2, like other CoVs is an enveloped, single-stranded RNA virus. The nanomachine, 50-200 nm in diameter, contains a large number of functional and structural proteins (such as, spike, envelope, membrane, nucleocapsid), the structures of which known to-date have been recently summarized by Kumar et. al.[6] The genome of the virus has been rapidly characterized.[7] Since then, mechanisms behind the virion's entry into the host cells have been an active field of research.[8-26] While SARS-CoV-2 is closely related to certain bat-derived CoVs (with 88% identity match), it is distantly related to SARS-CoV-1 (77% identity). Yet, both the SARS variants utilize a common host receptor, peptidase domain (PD) of the angiotensin-converting enzyme 2 (hACE2) to invade human cells via its spike (S) glycoprotein, protruding from the viral surface. The primary physiological role of hACE2, expressed in many organs including the lung, small intestine, testis, and kidney,[24, 27] involves the maturation of angiotensin, which is a peptide hormone that regulates vasoconstriction and blood pressure.

The S protein has two major subunits, S1 and S2. The S1 subunit plays a role in receptor recognition and binding while the membrane-anchored S2 subunit mediates the fusion of the viral and the host cell membranes. The S1 subunit has two well-defined structural domains, the receptor binding domain (S/RBD) and the N-terminal galectin-like domain. The S/RBD undergoes hinge motions that transiently undergo down and up conformational changes.[16] While the "down" confirmation refers to receptor inaccessible, the "up" conformation is conducive to the receptor binding.[28, 29] Recently, multiple μs-long all-atom molecular dynamics (MD) simulations have demonstrated that beyond shielding the SARS-COV-2 S, the highly dense

glycans also play a decisive role in controlling the RBD conformational switch over utilizing the N-glycans linked to N165 and N234.[30] This dynamical switch over might explain the hACE2 binding affinity of the entire SARS-CoV-2 spike is comparable to or lower than that of the SARS-CoV-1 spike protein. The inaccessible down conformation of the SARS-COV-2 S/RBD might also be responsible for evading innate immune surveillance.[19] Only six out of fourteen residues that the SARS-COV-1 S/RBD known to interact with hACE2 are mutated in the SARS-COV-2 S/RBD. These mutated residues interact more favourably with the viral binding host spots on hACE2 leading to a higher binding affinity for the SARS-COV-2 S/RBD[12, 22] while in "up" conformation. Leakage of the genetic material from the viral envelope to the human cell is finally triggered by the proprotein convertase furin. The hide and seek roles of the S/RBD, its higher binding affinity with the hACE2, and the furin preactivation of the SARS-COV-2 S work in unison and are believed to be the main causes behind the contagion's high infectivity.[19]

Barely a year after the SARS-COV-2 genome is mapped,[7] the breakneck speed with which the researchers around the world thrives to put an end to the crisis has even led to the opening up of a COVID literature database.[31] Being the first stage of cellular infection, dismantling the S/RBD-hACE2 interaction is an extremely attractive therapeutic target.[32] The structure of the S/RBD in complex with hACE2 has been solved by X-ray diffraction and cryo-TEM techniques by various groups.[12, 22, 24] Molecular modelling and simulation studies have also been performed to provide a comprehensive view of the S/RBD-hACE2 interactions and traced back to the formation of a dense hydrogen bond (HB) network between the interacting partner. [8-11, 13-18, 20, 21, 23, 33] Different therapeutic strategies are envisaged targeting the S/RBD.[32, 34] Peptide analogues,[25, 35-39] antibody,[40-49] and nanobody[50] as RBD inhibitors are at the center stage of research. Common to all of them is the strategy that the inhibitor under investigation recognizes an epitope that overlaps with hACE2 binding sites in S/RBD. A variety of vaccine development projects also evolves around blocking the S/RBD.[51]

Previous studies revealed that a large number of antibodies (Y-shaped protein) showed neutralization activity by targeting the RBD of other CoVs variants (SARS-CoV-1, MERS) and thereby disengaging the virus-receptor interaction.[52-54] Although the clinical effectiveness of convalescent plasma therapy, containing antibodies is remarkable,[41] its widespread use is limited by the large-scale production of plasma. However, neutralizing monoclonal antibodies (mAbs) isolated from B lymphocytes (B-cells) of the adaptive immune system is a promising alternative towards prophylactic and therapeutic treatment due to their scalability. A large number of COVID-19 antibodies are on trial [40] and several S/RBD-bound antibody crystal structures are known.[42, 43, 47, 49, 55] Recently an *in silico* mutagenesis protocol has been developed to enhance the potency of a known antibody.[45] Single-domain antibodies, also known as nanobodies (Nbs), with smaller size, good solubility, strong stability, and similar specificity and affinity

towards the target offers an attractive therapeutic alternative. They can be easily produced in large quantities in Escherichia coli and yeast cells at much cheaper costs. Their half-life can also be readily increased by oligomerization. A large number of neutralizing Nbs presently are at the preclinical stages of development.[46] One such Nb (named, Ty1) derived from alpacas has been successfully attempted to neutralize the SARS-COV-2 S/RBD both in the 'up' and 'down' conformations.[50] Advantages of peptide inhibitors include high specificity, less likelihood of eliciting an immune response, and faster FDA approval times,[56] could potentially also be used as an inhaler for topical lung delivery.[57] Like peptide inhibitors, Nbs can be delivered via aerosols so that they can reach the airway epithelia directly. Vaccine development programs, on the other hand, are although fast-tracked[51] and a few of the developed vaccines are in circulation, vaccinating the entire world population looks like at least for the time being, a far-fetched dream. To date, only 363 million vaccine doses have been administered [5] versus a world population of ~ 7.8 billion people.[58] Prophylactic and/or therapeutic anti-viral drugs will continue to be an indispensable tool before community protection through large-scale vaccination programme is in place or for those individuals who either refuses to administer the vaccine or respond poorly to vaccination.

In this study, we present findings from MD simulations of binary protein complexes of the RBD domains of the SARS-COV-2 S-protein with the natural receptor hACE2, antibody B38, and a nanobody Ty1. Analysis of the dynamic trajectories reveals a hydrophobic region, a dense and delicate hydrogen-bonding network at the binding interface in all the three protein complexes. A detailed comparison of the interactions as a function of the interfacial separation of the S/RBD-hACE2 complex with those in S/RBD-B38 and S/RBD-Ty1 guided us to advocate one key mutation (F27Q in the heavy chain) in the mAb B38 and to design a Ty1-based designer peptide. Both the mutated Fab (mFab) and the designer peptide are found to interact more strongly with S/RBD and can even outclass the S/RBD-hACE2 binding. The results are based on metadynamics[59] simulations of the complexes by employing center of mass (COM) separation of the interfacial residues as a collective variable (CV). All the binding basins of the complexes along the CV (COM separation ranging from 5 to 40 Å) are characterized. The characterization of the binding basins further confirms that the mFab and the designer peptide recognizes epitope sites in the S/RBD overlapping the binding site of ACE2 even more firmly than their wild variants, suggestive of efficacious blocking effect and neutralizing capacity. The present *in silico* approach provides guidance for the design of protein-based antivirals with higher affinities and enhanced epitope recognition.

2. Methods

2.1. All-Atom Simulations of SARS-COV2-S/RBD in Complex with hACE2 and Inhibitors. The initial coordinates of the SARS-COV-2 S in complex with hACE2 (PDB ID: 6lzg),[22] B38 (PDB ID: 7bz5),[47] and Ty1 (PDB ID: 6zxn)[50] are taken from the protein data bank. Missing residues and atoms were fixed with the "pdbfixer" tool of the openmm program.[60] Amino acids of the proteins were protonated corresponding to serum pH conditions (pH=7.5) by the H++ server.[61] All-atom MD simulations are performed with Gromacs-4.5.5 software.[62] The topology of the protein is built with the amber99 force field (AMBER99SB-ILDN).[63] After preparation of topology, each of the complexes is solvated by employing a three-point TIP3P water model.[64] An appropriate number of Na^+ and Cl^- atoms are added to neutralize the system and mimic a physiological salt concentration (0.15M). The energy of the solvated and charge neutralized systems are minimized successively using the steepest descent conjugant gradient methods. The systems are gradually heated to reach a temperature of 300 K. First, the water molecules are equilibrated by maintaining their temperature at 300 K, then the temperature of the added ions and protein molecules are sequentially increased to 300 K. The integration time step is 2 fs with the linear constraint solver (LINCS) [65] algorithm being used. Berendsen's external bath method with 1ps coupling time is used to maintain 1 atm pressure of the system.[66] 1 ns simulation is performed in the canonical thermodynamic ensemble (NVT), where the temperatures of the water, ions, and protein are independently coupled to a 300 K temperature bath using a velocity rescaling algorithm.[67] Particle mesh Ewald (PME)[68, 69] method is used for calculation of long-range electrostatics. A cut-off of 12 Å is taken for long-range electrostatics as well as the van der Waals non-bonded interactions. Finally, equilibrium MD simulations are performed for 10 ns for each of the systems in isothermal-isobaric NPT ensemble conditions at 1 atm and 300 K.

2.2. All-Atom Simulations of SARS-COV2-S/RBD in Complex with Designer Inhibitors. The designer inhibitors (mutated B38, and the Ty1-based peptide) are prepared as follows.

Mutated B38. The key amino acid of B38 to be mutated (F27 in the heavy chain) is replaced with the corresponding mutant residue (Q27) in the sequence of the residues. The original coordinates of the amino acid to be mutated are removed from the structure and in place, the coordinates of the mutant are generated using the "pdbfixer" tool of the openmm[60] programme and the resulting structure is optimized. Equilibrium simulation of the mutated B38 in complex with S/RBD is conducted following the same protocol as depicted above.

TY1-based peptide. Residues 3 to 6 (QVQL), 28 to 36 (GFTFSSVYM), 44 to 57 (GLGPEWVSRISPNS), and 102 to 112 (LNLSSSSVRGQ) of TY1 are selected to design the peptide inhibitor. Selected residues

are joined together by peptide bonds between residues 6 and 28, 36 and 44, 57 and 102 as follows. C-terminus of the L6 is joined with the N terminus of the G28; C terminus of the M36 is joined with N terminus of G44; and C terminus of S57 is joined with N terminus of L102 making peptide bonds between these residues using chimera software.[70] We place the peptide in the initial position known from the equilibrated structure of Ty1 in complex with S/RBD (cf. PDB: 6ZXN). The designed peptide is then docked at the spike protein interface using metadynamics method [71] in physiological solution. The method (see below) when used in flexible docking, ensures energy minimized docked geometry even without assuming previous knowledge of the docked geometry. Two features, namely, the reduction in the dimensionality of the search through the introduction of a suitable CV, and the possibility to obtain the free energy while on the go make metadynamics a versatile tool for docking. COM separation between the interfacial HB forming residues of the S/RBD and designer peptide is chosen as CV, along which the Gaussian bias is added. Gaussian hills of width 0.05 nm and initial height 0.50 kJ/mol are added at 5 ps intervals with a bias factor of 15 during the metadynamics run. The use of phase space accessible during the docking is limited between 0.2 to 1 nm by the introduction of a restraining potential at the boundaries.[72] The minimum of the free energy profile along the CV is chosen as the docked geometry of the complex, which was then subjected to a restraint-free 10 ns equilibrium run.

Finally, the five well-equilibrated solvated systems of the protein−protein complexes are used for subsequent enhanced non-equilibrium simulations (metadynamics)[59] to capture the rare unbinding events efficiently within a reasonable computational time.

2.3. Well-Tempered Metadynamics. Well-tempered version of metadynamics is adopted to circumvent the inherent nonequilibrium nature of a biased simulation by rescaling the hill height (W) of the added Gaussians along chosen CV as,

$$W = \omega_0 \tau_G e^{-V_G(CV,t)/k_B \Delta T},$$

where ω_0 is the initial deposition rate, τ_G is the deposition stride, $V_G(CV,t)$ is the bias potential accumulated in CV over time, t, and k_B is the Boltzmann constant. Gaussian at every 500 time steps with height of 1 kJ mol^{-1} and width 0.05 nm are added along the chosen CV. The bias factor γ [$(T + \Delta T)/T$] is taken as 15, and all the simulations were carried out at a temperature of 300 K. All the metadynamics runs are carried out by utilizing PLUMED plugin[72] to the Gromacs suite of the MD program.[62] The COM separation (the chosen CV) between the HB forming interfacial residues of the protein-protein complexes are allowed to vary between 0.5 nm to 4 nm during the simulation by employing restraining potential walls at the boundaries. After the simulations are converged, the free-energy profiles along the CV are calculated directly by post-processing the added hills by utilizing the *sum_hills* facility of PLUMED.[72]

To ensure convergence of the free-energy profile in the discovered binding basins, additional analyses are performed: (i) the height of the Gaussian hills as a function of time, which are seen to approach a value close to 0 at the times as indicated and at times sufficiently long thereafter (see SI, Figure S2). This is a signature of complete diffusive behaviour of a system in the explored phase space; (ii) PMF profiles at different time intervals, which are aligned by setting the global minimum to zero (see SI, Figure S3), and the PMF profile in the discovered basins are found to be unaltered well before the metadynamics runs are terminated; (iii) Additionally, the time evolution of CV space for S/RBD-B38 (Figure S4) and S/RBD-mutated B38 complex (Figure S5) are monitored. Efficient exploration of the CV space, especially in and around the reported binding basins can be seen.

To explore the binding features at each of the basins (total 15) of the five S/RBD-inhibitor complexes, first a 100 ns equilibrium simulations are conducted in each of the basins. Then five parallel runs (15 ns each) for each of the basins are then performed extracting configurations at 20, 40, 60, 80, and 100 ns of the initial 100 ns run. All the simulating systems are listed in Table S4 in the Supporting Information.

HB is calculated using the *g_hbond* plugin of Gromacs. Based on geometric criterion, a donor (D) and an acceptor (A) are said to be hydrogen-bonded when the distance between them is less than 3.5 Å and the D−H−A angle is less than 35°. Root mean square deviations and potential energies are evaluated using *g_rms* and *g_energy* plugins of Gromacs, respectively. While Van der Waals contacts are counted for separation of atoms less than or equal to 4 Å utilizing the *g_mindist* facility of Gromacs.[62]

3. Results and Discussion

3.1. SARS-CoV-2 S/RBD Binding Interface with hACE2. The S1 subunit of the S-protein contains an N-terminal domain (with no affinity towards hACE2) and the RBD (residue numbers 335 to 515) in the C-terminal domain, where the receptor binding motif (RBM, spanning between residues 437 to 508) is responsible for the interaction with the hACE2 to gain entry into the host.[22, 24] The concave surface of the RBM with a ridge loop on one side binds to an exposed convex surface of hACE2. A large binding interface of hACE2 comprising mainly of N-terminal helices (residue numbers 18 to 90) with secondary interaction sites (residue numbers 324 to 361) interacts with the RBM of SARS-COV-2. Several MD studies have revealed the molecular details of RBD-hACE2 interactions and identified the molecular traits responsible

for the enhanced binding capacity of SARS-COV-2 with hACE2 than the SARS-COV-1 variant.[11, 15, 21, 23, 33] Binding of hACE2 with the SARS-CoV-2 S/RBD is largely driven by electrostatic interactions with a delicate network of H-bonds, hydrophobic contacts, π-π and cation-π interactions.[36] Sequence variations between the RBMs of the two SARS variants mainly aggregate in the loop regions. Two of these loops are located at the two ends of the contact region (CR) in the receptor-bound complex, denoted as CR1 and CR3, while the middle region (CR2) consists of two short β strands bridging across the N-terminal helix of hACE2.[23]

The loop in the RBD's CR1 (residue numbers 470 to 489) is more rigid comprising of a well resolved secondary structure composed of small β sheets.[21] In particular, insertion of G482 makes the loop longer and converts the residues in CR1 an effective recognition motif in the hACE2 receptor complex, exemplified by a large number of H-bonds and van der Waals (vdw) contacts with the receptor residues (Table 1). Namely, S19 and Q24 of hACE2 form intermittent H-bonds with A475, G476, S477, and N487 of the RBD. Y83, a hot spot residue in the receptor[38] forms persistent H-bonding interaction with N487. Almost all the residues in CR1 make vdw contacts with the receptor, contributing significantly to the binding. In supporting information (SI), Table S1 the complete list of the vdw contacts of the crystal-bound complex is provided. The increased flexibility of SARS-COV-2 due to four mutations out of five proline residues in a short peptide sequence (472 to 483) of SARS-COV-1 makes F486 in CR1 a principal hydrophobic anchor for the RBM.

A number of residues are mutated in the CR2 region [R(403)-K(417)-N(452)Y(453)-L(455)F(456)-Q(493)S(494)] of SARS-COV-2 from SARS-COV-1.[21] For example, K417/V404, L455/Y442, F456/L443, Q493/N479 in SARS-COV-2/ SARS-COV-1 RBM differs that contributes significantly to the enhanced binding affinity of SARS-COV-2. Most importantly K417 in SARS-COV-2 creates a positive electrostatic patch along the binding interface, which plays a significant role in enhanced hACE2 binding by forming a strong salt bridge with the nearby hACE2 residue, D30 (Table 1). H34 in hACE2 enjoys a rich network of H-bond with the CR2 residues, R403, K417, Y453, and Q493, rendering it to be another binding hot spot.[38] Similar to this, K31 and E37 in the receptor can be identified as hot spot residues[13] for their persistent H-bond with Q493 and R403 RBM residues, respectively. Residues spanning the CR2 region are also in an extensive network of vdw contacts with hACE2 interfacial residues (see SI, Table S1).

Q498, T500, and N501 of CR3 [Y(449)-Q(498)PTNGVGYQP(507)] are at the center of H-bond network (Table 1), anchoring the RBM at the N-terminal helix of hACE2. All the residues in CR3 are also

found to be engaged in extensive vdw contacts at the interface with the receptor (SI, Table S1). A recent computational alanine scanning study has identified Q498 and T500 as binding hot spots on the RBM.[13] D38 and Q42 of the receptor forms simultaneous H-bonds with Y449 and Q498 residues of the RBM. Interestingly, Q42 is also found to be involved in direct H-bonding interactions with G446 and G447 residues of the RBD, not classified in any of the three contact regions (CR1 to CR3). Similarly, Y41 (receptor) forms simultaneous H-bonds with Q498 and N501 residues of the RBM in association with a large number of vdw contacts between them. Likewise, K353 (receptor) is engaged in H-bonding interactions with N501 and G502 RBM residues. While T500, N501, and G502 RBM residues form simultaneous H-bond with D355 receptor residue at the binding interface. Such a rich network of H-bonding contributes to the higher binding affinity of SARS-COV-2 with hACE2.[23]

In summary, the equilibrium MD simulation of the crystal structure of the S/RBD-receptor complex provides qualitative insights into its interfacial interactions determining the shape and stability of the complex, which is largely dominated by electrostatic and vdw interactions. Given the low dielectric constant (~4) inside the protein, K417(RBM)-D30(hACE2) ionic interaction yields a strong electrostatic environment across the central hydrophobic contact region. Recent molecular mechanics Poisson-Boltzmann surface area calculation estimated binding free energy contribution by K417 alone is ~ −12.34 kcal/mol towards the total electrostatic contribution (~ −746.69 kcal/mol) of the complex. Vdw contribution towards the binding free energy is estimated to be ~ −89.93 kcal/mol.[11] Here we have identified in total 17 residues of RBD and 16 residues of hACE2 as interfacial residues in the protein-protein complex-forming H-bond, one salt bridge, and several vdw interactions (Table-1). The potential of mean force (PMF) during the unbinding of the complex is explored along the CV defined as the variation of distance between COM of the interfacial residues of RBM and the one on the hACE2.

3.2. SARS-CoV-2 S/RBD Binding Interface with Antibody, B38. The H-bonding and vdw interactions at the interface of the Fab-RBD complex are tabulated in Table 2 and SI, Table S1. Both the variable regions of the heavy and light chains of the Fab interact with the RBD. Notably, both of the B38 chains in complex with RBD exhibit C_α root-mean-square deviation (RMSD) within 1.5 Å from the starting crystal structure, indicating no significant conformational changes and stable complex during the simulation (Figure S1). Like in the crystal structure of the complex,[47] present MD simulation in explicit water also finds three complementarity regions (CDR) on the heavy chain (HCDR) and two CDRs on the light chain (LCDR), constituting the paratope on the antibody. The residues in the three HCDRs loops are; HCDR1: [G(26)-I(28)- S(30)-S(31)-N(32)]; HCDR2: [Y(52)-Y(58)]; HCDR3: [R(97)-Y(100)-D(103)]. While LCDR loops are constituted by; LCDR1: [I(29)-S(30)-Y(32)]; LCDR2: [Q(90)-L(91)-N(92)-Y(94)]. It can be seen in

Table 2 that in parallel with the RBD-hACE2 complex (Table 1), the paratope residues of B38 interact with RBD in all the three contact regions (CR1-CR3). That is, the paratope on the antibody binds the same epitope of the RBD as the hACE2, explaining the blocking effect and neutralizing capacity. LCDRs and HCDRs of the Fab predominantly interact with the RBD in the CR3 and CR1 region of the RBD-hACE2 complex, respectively, while in the CR2 region both the CDRs interact. Like in the RBD-hACE2 complex, a crucial and stable salt bridge is found to be formed between K417(RBD) and E98 (B38 heavy chain). This salt bridge and several other non-CDR residues (e.g. Y33 of the heavy chain forms three stable H-bonds with K417, Y421, and L455 of the RBD) hold the CDRs tightly bound to the RBD. S30 and Y32 of LCDR1 and N92 of LCDR2 are involved in a rich network of H-bonding, forming at least four H-bonds by each of them with RBD residues. Similarly, each of the residues G26, S31 of HCDR1, and R97, Y100 of HCDR3 enjoys at least two H-bond interactions with the RBD (Table 2). In addition to the rich network of H-bonds, dense vdw contacts at the Fab-RBD interface ensure a stable complex. Out of the 17 RBD residues at the interface in the RBD-hACE2 complex, 14 residues interact with B38, explaining the blocking effect and neutralising capacity of the Fab.

In total 34 residues of RBD interacts with B38, out of which 16 residues with heavy chain and 17 residues with the light chain, while one residue (K417) with both the chain of the Fab are engaged in the interfacial network of interactions (Table 2). On the other hand, 17 residues of the heavy chain and 13 residues of the Fab light chain participates in the interfacial interactions with the RBD. COM separation between the interfacial residues of the RBD and the heavy and light chains of B38 is considered to be the CV during unbinding simulation.

3.3. SARS-CoV-2 S/RBD Binding Interface with Nanobody, Ty1. In Table 3 we have listed the H-bond interactions of the RBD-Ty1 complex and the full list of vdw interacting residues of the two proteins are provided in Table S1. The RMSD of the Cα atoms of the nanobody differs only ≈ 1.5 Å from the crystal structure in the course of the simulation, indicating a stable complex in an explicit water environment (Figure S1). Like B38 in the RBD-B38 complex, three CDRs of the nanobody are known to constitute the paratope[50]: CDR1 (28GFTFSSVYM36), CDR2 (52RISPNSGNIGY62), and CDR3(99AIGLNLSSSSV109). The simulation results show that CDR1 and CDR3 together block the CR1 region of the RBD to a great extent via interfacial H-bonding. However, only one residue (Q493) in the RBD's CR2 region is found to be engaged interacting with two CDR3 serine residues of Ty1. Similar to this, only one residue (Y449) of RBD's CR3 is blocked by non-CDR residue (R110 and Q112) of the nanobody through H-bonding (Table 3). Residues in RBD's CR2 and CR3 regions are mainly engaged in vdw interactions with the nanobody (Table S1). Moreover, residues in CDR2 of the nanobody make no

major interactions (except a few vdw interactions involving residues 52 to 57 and one H-bonding utilizing N56) with the RBD but stabilizes the conformation of CDR1 and CDR3 in the RBD bound complex. N103 and Q112 of Ty1 form an extensive H-bonding networks. However, no salt bridge, one of the hallmarks of RBD-hACE2 or for that matter RBD-B38 interactions, is found to be formed by K417 of the RBD in the bound state with TY1. While 14 RBD interacting residues are common in the interface with hACE2 and B38, such commonality is reduced to 5 in the RBD-Ty1 complex. This might explain higher IC_{50} of TY1 (0.77 μg/ml)[50] and hence weaker binding affinity of Ty1 for RBD than that of B38 (IC_{50} = 0.177 μg/ml).[47] Since it is desirable to obtain inhibitors with their potency being as high as possible due to the binding competition with hACE2, here one of our principal goals is to design a peptide inhibitor from Ty1 that maximally recognizes the epitope site in the RBD overlapping the binding site of ACE2.

In total, 18 residues of RBD interact with 15 residues of the nanobody both by H-bonding and vdw interactions at the protein-protein interface (Table 3). COM separation between these interfacial residues is chosen as a CV in subsequent metadynamics run.

3.4. Unbinding of hACE2 and Inhibitors from the Binding Interface with SARS-CoV-2 S/RBD. To assess the binding affinities of hACE2, B38, and Ty1 with the RBD, we have conducted unbinding simulations of the protein complexes by applying an enhanced sampling technique, namely, a well-tempered version of metadynamics.[59] In Figure 1, the converged PMF profiles (for the convergence of the simulations see SI, Figures S2-S5) of the unbinding events along the chosen CV, namely, COM separation between the interfacial residues are presented. During unbinding, old interactions break apart to give rise to newer ones, leading to multiple barriers and local minima (basins). Because a large number of residues are involved in the interface, the interaction does not vanish even at 4 nm of COM separation However, the PMF profiles for the unbinding events of the three protein complexes are different from each other as is evident in the Figure. For example, while hACE2 exhibits four binding basins, B38 and TY1 exhibit two and three binding basins, respectively along the unbinding pathway. The position of basin 1 appears at ~0.75 nm along the RBD-hACE2 and RBD-B38 interfacial COM separation, but that in the case of RBD-Ty1 complex is found to be ~0.55 nm. The depth of the energy minima at basin 1 (Figure 1) of the three complexes implies a higher affinity of hACE2 (deepest binding free energy minimum), followed by B38 and TY1 towards RBD in their bound states. Thus amongst the three bound complexes, although the nanobody approaches closest to the RBD interface, its interactions are less favourable than those prevailing at the RBD-hACE2 and RBD-B38 interfaces. The positions of the interfacial separations at the most stable binding basins of the three RBD complexes are also different (hACE2: basin 3 at 1.55 nm; B38: basin 2 at 1.75 nm; Ty1: basin 3 at 2.5 nm). As is evident in Figure 1, in order to approach further closer to the RBD

interface, hACE2 has to surmount an energy barrier of ~ 50 KJ/mol to be trapped in basin 2 from where it can reach basin 1 by overcoming a much weaker barrier. On the other hand, B38 while approaching binding basin 1 from basin 2 faces a larger free energy barrier (~100 KJ/mol). While for the nanobody, the bound structure at basin 3 has to first surmount an energy barrier of ~ 50 KJ/mol to reach binding basin 2 at 1.75 nm COM separation and then a much larger barrier (> 150 KJ/mol) to form the RBD-TY1 complex at the closest interfacial separation at basin 1. These observations again point to the fact that RBD has the highest affinity towards hACE2 in comparison to its two inhibitors (B38 followed by Ty1). Below we further characterize the binding basins of the three complexes. Structures of each of the complexes in their binding basins (RBD-hACE2: 4, RBD-B38: 2, RBD-Ty1: 3, *cf.* Figure 1) are extracted from metadynamics simulation and each of them is then subjected to 100 ns equilibrium simulations. Five parallel runs are carried out based on the simulation configurations at 20, 40, 60, 80, and 100 ns (see Methods for details). The five parallel simulations are employed to calculate potential energy (sum of interfacial short-range Coulomb and Lennard-Jones interactions), interfacial H-bonds, and vdw contacts of the protein-protein complexes in their binding basins (see SI, Table S2).

3.4.1. RBD-hACE2 Binding Basins. In Table 4, residues participating in H-bond interactions between the RBD and hACE2 at the four intermolecular binding basins are listed. In Figure 2, snapshots of the structures in the for bound states are provided. As the COM separation between the interfacial residues progressively increases, the binding basins along the unbinding pathway exhibit observable differences. The potential energy of binding at basin 1 is -950 ± 51 kJ/mol (SI, Table S2). An increase in interfacial separation by ~0.2 nm from basin1 to basin 2 (Figure 1) compromises RBD-hACE2 interaction by 55% to -425 ± 50 kJ/mol. Similarly moving to basin 3 at 1.55 nm, the interaction is reduced by 95 % to settle at -45 ± 3 kJ/mol and further to basin 4 at 2.25 nm, the interaction energy almost vanishes to -5 kJ/mol. In line with this, the number of intermolecular H-bond reduces from 51 (basin 1) to 1 (basin 4). However, the number of vdw contacts remains sizeable (77) even at basin 4 (from 632 in basin 1). This may imply that when the two proteins approach each other from a distance it is the vdw interactions that first induce attraction between them leading to successful interfacial binding dominated by electrostatic interactions with a delicate network of H-bonds, hydrophobic contacts.

All the three contact regions (CR1 to CR3) of the RBD, like in the RBD-hACE2 crystal structure, are found to be interacting even until basin 2 (Table 4). For example, Y83, previously identified as a hot spot residue in receptor[38] continues to form persistent H-bonding interaction with N487 in the CR1 region. Similarly, S19 (in basin 1) and Q24 (in basins 1 and 2) of hACE2 are in the H-bond network with A475, G476, S477, and N487 in the CR1 region of the RBD. Most noticeably the pivotal K417-D30 salt bridge

of the interfacial arch at CR2 remains unperturbed until basin 2. However, H34 in hACE2 (another hot spot residue)[38] loses the H-bond with R403, while its H-bonds with another CR2 residue, Q493 remained intact until basin 2 is reached. Similar to this, while amongst K31 and E37 (hot spot residues)[13], the former enjoys H-bond interaction with Q493 until basin 2, the latter loses the said interaction with R403 immediately after basin 1. In the CR3 region, Q42 of the receptor is the first residue with which G502 of the RBD begins anchoring the RBM with the N-terminal helix of hACE2 when the two proteins approach each other from a distance (see basin 4 in Table 4). In basin 3, Q42 loses its contact with G502, and H-bond with nearby Y505 forms in place. This H-bond switchover helps in anchoring E35 (receptor) with the K417 (CR2) of the RBD residue by forming a weak salt bridge. Moving closer to basin 2, the two receptor residues active in basin 3 change their role. Namely, Q42 establishes contact with N501 and E35 with R403; while the weak K417-E35 salt bridge is broken, a strong salt bridge K417-D30 appears. Moving even closer to binding basin 1, like in the crystal bound state, D38 and Q42 of the receptor form simultaneous H-bonds with the CR3 residues, Y449 and Q498. Likewise, in basin 1, K353 (hot spot receptor residue)[38] is engaged in a rich H-bonding network with Q498, N501, and G502 RBD residues.

3.4.2. RBD-B38 Binding Basins. In Table 5, Figure 3, and SI Table S2 the binding features, structure and energetics of the two binding basins of the RBD-B38 complex are enumerated. The potential energy between the RBD and the Fab at basin 1 (interfacial COM separation ~0.8 nm) is -810 ± 14 kJ/mol. In moving to the second basin at 1.75 nm interfacial separation, the potential energy reduces by 90 % to settle at -81 ± 4 kJ/mol. In concomitant with this, the number of H-bonds decreases from 85 ± 2 to 20 ± 1. However, the number of vdw contacts increases to 1359 ± 48 from 1033 ± 75 (Table S2). This result again points to the fact that when the Fab approaches from a distance, a large number of vdw contacts and several H-bonds (Table 5) primarily from the HCDR1 and HCDR3 of the Fab anchors with the CR1 region of the RBD (viz. RBD-hACE2 complex) in basin 2. Y32 of LCDR1 forms a weak H-bond with K417, which subsequently breaks, and the crucial salt bridge K417 (RBD)-E98 (Fab heavy chain) forms when the two proteins come closer at basin 1. At basin 1, the paratope on the antibody (HCDR1 to HCDR3 and LCDR1 and LCDR2) binds the same epitope of the RBD (CR1 to CR3) that recognizes hACE2. While in basin 2, the heavy chain of the Fab enjoys a large number of H-bonds with the RBD as compared to the light chain (19 versus 1), in basin 1, the light chain of the Fab is found to be engaged with a larger number of H-bond interaction than the heavy chain (46 versus 39). In basin2, HCDR residues N32 (HCDR1) and Y100 (HCDR3) are in the H-bond network with the RBD residues Q474, S477, and N487. This H-bond network breaks apart to give rise to newer ones at basin 1 where the Fab light chain is seen to establish contact with the RBD chain. For example, each of the residues, such as, G26 and S31 of HCDR1, S53, G54, S56 of

HCDR2, R97 and Y100 of HCDR3 forms at least two H-bonds with the RBD, which also includes CR1 residues that are known to interact with hACE2. S30 and Y32 of LCDR1 form multiple H-bond contacts with residues in the CR3 and CR2 region of the RBD, respectively. Whereas, N92 of LCDR2 enjoys multiple H-bond contacts with the RBD residues; CR2: R403, K417, and Y453, CR3: Y505.

3.4.3 RBD-TY1 Binding Basins. The three binding basins of the RBD-nanobody complex (Figure 1) are characterized in Table 6, Table S2, and Figure 4. The potential energy of interaction, in particular, the short-range Coulomb interaction in the most tightly held binding basin (basin 1) is seen to be the least in the RBD-TY1 complex (-168 ± 5 kJ/mol) when compared with either RBD-hACE2 (-706 ± 51 kJ/mol) or RBD-B38 (-563 ± 23 kJ/mol) complexes. The weak electrostatic complementarity of Ty1 may explain its weaker binding affinity for the RBD. When the two proteins approach each other from a distance, residue S107 (CDR3) of Ty1 with polar side chain first recognizes E484 and F486 residues of RBD by forming H-bonds. Simultaneously a weak salt bridge E484(RBD)-R110 (Ty1) is seen (Table 6) at the farthest basin (basin 3). Coming closer to basin 2, the salt bridge between the proteins breaks down, S107 continues to H-bond strongly with E484 by acting both as donor and acceptor of hydrogen. A non-CDR residue, Q112, which is found to interact with G482 (RBD) in basin 3, changes its H-bonding partner to Y351 and T470 of the RBD in basin 2. In basin 1, Q112 enjoys extensive H-bonding with several adjacent RBD residues: 444KVGGNYN450. Similar to this, N103 (CDR3) with its polar side chain makes multiple H-bond contacts with nearby RBD residues: 484EGFN487 (CR1). However, CR3 (barring Y449) and CR2 (barring Q493) regions of the RBD are found to be mainly unoccluded.

After investigating the molecular mechanism of the two inhibitors' binding with the RBD, both in their crystal structures and in several binding states discovered during the unbinding simulations, we now endeavour to design more potent inhibitors. Here one of our principal focuses is to design inhibitors with maximum recognition of the epitope that overlaps with hACE2 binding sites in the RBD (CR1 to CR3). Our designed mAb through protein mutagenesis of B38 and a designer peptide inhibitor, which included components from the RBD-binding domain of the nanobody is seen to accomplish the task of maximum epitope recognition. In addition, the energetics of the inhibitor-RBD complexes are also suggestive of the designed inhibitors' enhanced affinity toward RBD (see below).

3.5. Mutagenesis of B38 and Equilibrium MD Simulation of the Mutated Fab in Complex with RBD. A comparison between Table 1 (RBD-hACE2) and Table 2 (RBD-B38) reveals that all the residues in the three contact regions of RBD with hACE2 are also engaged in H-bond interaction with B38 CDRs, except

G476 of the RBD at CR1. This interfacial residue forms strong H-bonds simultaneously with S19 and Q24 of hACE2. Further, Q24 also interacts with the other CR1 residues in the RBD both in bound crystal structure and also along the binding basins (1 and 2) during metadynamics simulation of RBD-hACE2 complex. On the other hand, in the crystal structure and the equilibrium simulation of the RBD-B38 complex, B38 residues within 5 Å separation from G476 (RBD) are found to be G26, F27, I28, S31, and N32 of the Fab heavy chain. It can be seen in Table 2 that all these residues forms H-bonds with the other CR1 residues of the RBD, barring F27. Although F27 makes some vdw contacts with certain RBD residues (Table S1). To mimic G476(RBD)-Q24(hACAE2) interaction in CR1, we have chosen to mutate F27 with glutamine having polar uncharged side chains. Thus the B38 mutant in this work is chosen to be F27Q in the heavy chain. Equilibrium MD simulation of the mutated B38 in complex with the RBD indicates a stable configuration in explicit water environment (Figure S1) as the RMSD of the Cα atoms of the mutated antibody (like its wild variety) differs only ≈ 1.5 Å from the starting structure in the course of the simulation.

The effects of this single mutation on the mutated Fab is seen in the interfacial interaction with the RBD. The H-bond interactions (Table 2) and the vdw contacts between the mFab and RBD (Table S3) during the equilibrium MD simulation of their complex show several encouraging signs. All the three CDRs constituting the paratope on the mutated antibody once again found to bind the same epitope of the RBD as the hACE2. The stable salt bridge between K417(RBD) and E98 (mFab) is found to be intact. Additionally, several other new interactions are seen to be developed. For example, the mutated residue, Q27 in HCDR1 now found to forming H-boning interactions with G476, S477 and T478 and N487 residues of the RBD. Y32 of LCDR1 and N92 of LCDR2 are involved in rich network of H-bonding, forming at least five H-bonds by each of them with RBD residues. Similarly, each of the residues I28, S31, N32 of HCDR1, and R97, Y100 of HCDR3 enjoys at least two H-bond interactions with the RBD (Table 2). Several non-CDR residues, such as, each of D0, G28, S30, S31 of the light chain and S53, S56 of the heavy chain of the mFab found to form H-bond with RBD residues in the interface. 16 of the 17 RBD residues interacting with hACE2 (cf. Table 1) also interact with mFab (in comparison to 14 of the wild Fab). As the unbinding simulation reveals (see below), the enhanced interfacial interaction in the RBD-mFab complex also induces improved binding free energy, which may help reduce the required dosage of mAb during the therapy.

In total, 37 residues of the RBD interact with mFAb. Out of these, 15 of them interact with the light chain, 19 with the heavy chain, and 3 (R408, K417, and Q493) interact with both the chains of the mFab. Similarly, out of the mFab residues that forms the interface with RBD, 15 are from light chain and 18 are from heavy chain. In the metadynamics simulation, COM separation between the interfacial residues of the RBD and the mFab is considered to be the CV.

3.6. Ty1-Based Peptide Inhibitor and Equilibrium MD Simulation of the Peptide-RBD Complex. Previously, from the analysis of the interacting amino acids at the RBD and Ty1 interface (Table 3) we found that 15 residues from Ty1 interact with RBD. They are [G(28)- T(30)-S(32)-S(33)-Y(35)] from CDR1 of the nanobody, N56 from CDR2, [N(103)-S(107)-S(108)] from CDR3 and six non-CDR residues [Q(3)VQL(6)], R110 and Q112. As discussed above, these residues make weaker interactions with the RBD when compared with either hACE2 or B38. To enhance binding with RBD, we have designed a peptide inhibitor by selecting components from Ty1, such that, it can effectively occlude hACE2 by recognizing the CR1 to CR3 contact region in the RBD-hACE2 complex. A closer look at the vdw contact list (Table S1) reveals that F29 and M36 CDR1 residues of Ty1 make vdw contacts with the RBD in CR1 region. CDR2 residue, P47 along with nearby residues, G44 and G46 make vdw contacts with the RBD in CR3 region. While several CDR3 residues L102, L104, S106, V109 along with G111 make vdw contacts with the RBD in CR2 region. Based on these observations, we select following components from TY1: [Q(3)VQL(6)], [G(28)FTFSSVYM(36)], [G(44)LGPEWVSRISPNS(57)] and [L(102)NLSSSSVRGQ(112)] and joined them together by peptide bonds to form a 38 residues peptide. In subsequent discussion we have kept the residue identification number in the designer peptide unchanged for the ease of comparison with its parent, Ty1. Note that certain residues in the peptide (e.g. S31, M36, L48 to S54, S105) do not make any contact with the RBD in the RBD-TY1 complex. But they are chosen in the designer peptide in order to attain sufficient chain length, which can maximize the interfacial interaction with RBD. The RMSD of the Cα atoms of the designer peptide in complex with RBD displays a slightly higher fluctuation when compared with its parent, TY1. However, the RMSD value is found to differ only ≈ 2 Å from the starting structure in the course of the simulation, indicating a stable complex in explicit water environment (Figure S1).

MD simulation of the RBD-peptide complex reveals enhanced interfacial interactions and are summarized in Table 3 and Table S3. Several interesting observations can be made from the comparison of the binding characteristics of RBD with the designer peptide and with the nanobody, TY1. First, 27 residues of the RBD (in comparison to 18 in RBD-Ty1 complex) are directly involved in the interfacial H-bonding with the peptide. Second, 15 of the 17 RBD residues that form interfacial interactions in RBD-hACE2 complex are also seen to be engaged interacting with the peptide (in comparison to 5 in the RBD-Ty1 complex). Third, R403, K417, Y453, Q493, and S494 residues of the RBD (cf. CR2 contact region in the RBD-hACE2 complex) are seen to interact with the designer peptide (in comparison to only Q493 residue in the RBD-Ty1 complex). Similarly, Y449, Q498, N501 and Y505 residues of the RBD (cf. CR3 contact region in the RBD-hACE2 complex) are seen to interact with the designer peptide (in comparison to only Y449 residue in the RBD-Ty1 complex). While in the CR1 region of the RBD, Q3 and R52 residues of the peptide forms rich H-bonding network (similar to N103, S32 and S33 residues of Ty1). Fourth, a salt bridge

involving K417 (RBD), which is the hallmark of interactions in the RBD's complexation with hACE2 and B38, is again seen to emerge with E48 (peptide). Thus the designer peptide inhibitor from the components of Ty1 can be seen to maximally recognize the epitope site in the RBD overlapping the binding site of hACE2, which may also raise its occluding capacity.

In summary, 27 residues of RBD interacts with 21 residues of the designer peptide, both by H-bonding and vdw interactions at the protein-protein interface (Table 3). COM separation between these interfacial residues is chosen as CV in the subsequent unbinding simulation.

3.7. Unbinding of mFab and the Designer Peptide from the Binding Interface with SARS-CoV-2 S/RBD. In Figure 5, the free energy profiles for the unbinding transitions of RBD in complex with mFab (upper panel) and the peptide (middle panel) are presented. Each of the two inhibitors are found to from three binding basins although their locations along the interfacial separation coordinate are different. When the proteins approach each other from a distance, the first shallow binding basin (basin 3) is found to be formed at 1.9 nm and 2.3 nm interfacial COM separation of the RBD-mFab and RBD-peptide complexes, respectively. Further closer, to reach the binding basin 2 at 1.1 nm, mFab has to surmount a 45 kJ/mol free energy barrier. In comparison, to reach the binding basin 2 at 1.7 nm, the designer peptide experiences a much lesser barrier (4 kJ/mol). The intermolecular configuration of each of the protein-protein complex at basin 2 can be finally trapped in the deepest free energy well at basin 1. While for mFab, binding basin 1 is found to occur at 0.8 nm, for the peptide it is at ~0.9 nm. However, to reach the bound state at basin 1, configuration at basin 2 of the RBD-mFab complex experiences a free energy barrier height 40 kJ/mol. While for the RBD-peptide complex the corresponding barrier height is found to be 15 kJ/mol. Most significantly, in comparison to their wild variants, mFab is found to form a 60 fold deeper free energy well, while the designer peptide forms a 100 fold deeper free energy well in their respective first binding basins in complex with the RBD. Moreover, both of the designed inhibitors' binding free energy well depth at basin 1 are seen to be deeper than that of hACE2 (see Figure 5 bottom panel), indicating they may outclass the binding affinity of hACE2 with the RBD.

Below we characterize each of the binding basins of the designed inhibitors' complex with the RBD by conducting five parallel equilibrium MD simulations (see Methods) of their corresponding configurations. Indeed, as discussed below, the calculated potential energy, intermolecular H-bonds and vdw contacts of the protein-protein complexes in their binding basins may indicate higher binding affinities of the designed inhibitors with the RBD.

3.7.1. RBD-mFab Binding Basins. In Table 5, Figure 6, and SI, Table S2 the binding features, structure and energetics of the three binding basins of the RBD-mFab complex are enumerated. The potential energy between the RBD and the mFab progressively decreases from -1072 ± 13 kJ/mol (basin 1) to -350 ± 34 kJ/mol (at basin 2) to finally settle at -281 ± 9 kJ/mol (basin 3) as their interfacial COM separation increases from 0.8 nm (at basin 1) to 1.9 nm (at basin 3) (Table S2). Similar to this, the number of intermolecular H-bonds also decreases from 85 ± 4 (at basin1) to 33 ± 3 (at basin 3). When the mFab approaches from a distance, a large number of vdw contacts and several H-bonds (Table 5) by both of its chains anchors the inhibitor with the RBD at binding basin 3. Light chain residue, Y94, in particular, forms a rich H-bond network with T415, D420, Y421, and N460 residues of the RBD. While the heavy chain primarily anchors with the CR1 region of the RBD (viz. RBD-hACE2 complex). Coming closer to basin 2, the light chain residues make contact with the CR2 and CR3 region of the RBD. The mFab heavy chain, however, engages itself more intimately making contacts in the CR1 region. S56 of the heavy chain finds five H-bonding partners with the RBD residues. Similarly, each of the two serine residues of the heavy chain, S31 and S53 make three H-bond contacts with the RBD. Likewise, of the light chain residues, Q27 finds four and N92 finds three intermolecular H-bonding partners with the RBD.

Approaching further closer at basin 1, the mutated antibody, like its wild-type variant (B38) binds the same epitope of the RBD (CR1 to CR3) that recognizes hACE2. E98 of the heavy chain forms the salt bridge with K417 (RBD). The total number of H-bond contacts by the heavy (light) chain increases from 18 (15) at basin 3 to 31 (24) at basin 2 to finally settle at 47 (38) at the binding basin 1. At basin 1, the H-bonding partners between mFab and RBD remained almost invariant from those in the B38-RBD complex. For example, each of the residues, such as G26 and S31 of HCDR1, S53, G54, S56 of HCDR2, R97 of HCDR3 finds the same RBD residues to make H-bonds as it is in the B38-RBD complex. Likewise, N92 of LCDR2 forms an additional H-bonding interaction with Q493 (RBD, CR2), in addition to those prevailing in wild B38 (namely, R403, K417, and Y453). The mutated residue, Q27 in the heavy chain of mFab, on the other hand, makes multiple H-bond contacts with RBD CR1 residues, namely, G476, S477, and T478. These additional interactions by Q27 in the CR1 region of the RBD renders mFab its higher binding affinity with enhanced epitope recognition ability (than B38), which may successfully occlude hACE2. Note that our principal goal behind the F27Q heavy chain mutation of B38 is to mimic the G476(RBD)-Q24(hACAE2) interaction in the RBD-mFab complex can also be seen to be achieved.

3.7.2. RBD-Peptide Binding Basins. The three binding basins of the designer peptide with the RBD are characterised in Table 6, Figure 7, and SI Table S2. The short-range potential energy of interaction is seen to be significantly enhanced in all the three biding basins of the RBD-peptide complex in comparison to

RBD-Ty1 (e.g. at basin 1: -908 kJ/mol for the RBD-peptide complex vs. -280 kJ/mol for the RBD-Ty1 complex). So also are the number of H-bond contacts between the inhibitors and the RBD (see Table S2, at basin1: 65 vs 45 for the RBD-peptide and the RBD-Ty1 complex, respectively). From a distance when the two molecules come closer, the peptide, primarily with the help of Q3 residue first anchors with the CR3 region of the RBD at an interfacial COM separation, 2.3 nm (cf. basin 3). At this separation, the peptide's R52 residue also plays a vital role by making simultaneous H-bonds with Y449 (CR3) and S494 (CR2) residues of the RBD. Coming closer to basin 2, both the residues (Q3 and R52) of the flexible peptide chain lose old contact with the RBD giving rise to new contacts in the CR1 regions. At this binding basin, the peptide's conformation contemplates the RBD's interface to fully cover its CR1 region by utilizing a large number of residues, such as, G44, G46, W49, S54, L102, and N103, which are seen to maintain their interactions with RBD's CR1 residues until basin1 is reached (Table 6). After successfully anchoring with the CR1 region, the peptide chain reorients such that CR2 and CR3 regions of the RBD can now be covered at basin 1. This ensures a full epitope recognition in the RBD-hACE2 binding interface by the designer peptide. Aided by the higher binding affinity with the RBD (cf. deep binding free energy well at basin 1, shown in Figure 5), the designer peptide could be a potential inhibitor for blocking and neutralising the antigen.

4. Conclusions

SARS-COV-2 binding to hACE2 is dominated by the RBD/hACE2 interface. Disrupting this interface has been one of the major therapeutic strategies ever since the COVID-19 disease outbreak. The present work provides an atomistic-based, reliable *in silico* structural and energetic framework of interactions between the two proteins as a function of their relevant interfacial separation. The results may aid the precise structure-based design of neutralizing inhibitors (biologics) for the highly infectious contagion. For example, since the RBD makes multiple contacts (CR1 to CR3) with the hACE2 through an extended surface, it is our tenet that small molecule drug[32] targeting a specific epitope region of the RBD will be insufficient to prevent RBD-hACE2 binding. Consequently, one of the intervention strategies could be the inhibitors having large binding interfaces which can block the entire RBD interface. The monoclonal antibody, nanobody, and peptide inhibitors developed over time hold the promise that they can quickly latch onto the RBD interface (in common with hACE2) and keep a strong hold on it. However, producing neutralizing mAbs/nanobodies cost-effectively, and at a commercial scale is a challenging task. Nevertheless, one mAb (B38) isolated from B-cells of the adaptive immune system and an alpaca-derived

nanobody (Ty1) is a promising alternative towards this goal. Accordingly, we have identified all different residues of RBD-B38 and RBD-Ty1 complexes that form most of the protein−protein interface and estimated the variation in the corresponding free energy of binding as a function of their interfacial separation. The discovered structure-energetics of the binding basins during the complexes' unbinding show that blocking the RBD is relatively more feasible by the chosen antibody, B38 in comparison to the nanobody, Ty1. However, none of the two inhibitors is found to exhibit higher RBD binding affinity than hACE2 in their most tightly bound state (basin1).

One of the major goals of this work is *in silico* design of more potent protein inhibitors having significantly higher binding affinity than hACE2 can dominate over hACE2 interface in latching onto the RBD, thwarting the infection. In this pursuit, we have conducted mutagenesis of B38 and have engineered a Ty1-derived peptide. A comparison between the interfacial interactions of RBD with hACE2 and B38 at their equilibrium bound state has guided us to design a higher-affinity variant of the antibody, containing one single amino acid change in the heavy chain (F27Q), which can bind to the RBD more tightly than either of its wild variant (60-fold deeper free energy well in the first binding basin) or hACE2 (18-fold deeper free energy well in the first binding basin of RBD-mB38 vs. RBD-hACE2 complex). On the other hand, based on the RBD-Ty1 interfacial interactions at its equilibrium bound state we have designed a 38 amino acid peptide inhibitor taking components from Ty1, which retains a conformation-matched bent shape to the RBD for its recognition and a full cover of the RBD surface. The designer peptide exhibits improved affinity for the RBD by up to 100-fold (100-fold deeper free energy well in the first binding basin in comparison to its parent, Ty1), and like B38 mutant, it can outclass the binding affinity of hACE2 with the RBD. In summary, by exploring the structural and energetic details responsible for protein-protein interactions as a function of their interfacial separation, we have optimized two known neutralizing agents, both of which can recognize all the epitope regions of the RBD and in addition exhibit higher affinity for the RBD than hACE2. We expect that the designed inhibitors are highly promising and deserve further in vitro/vivo verification.

While preparing this work, the government authorities around the globe are issuing emergency use authorization for some of the available COVID-19 vaccines to break the infection chain. However, the rapidly spreading SARS-COV-2 variants due to fast viral diffusion and host adaptation may jeopardize the vaccine countermeasure.[73, 74] With or without such unfortunate and unforeseen situations, protein-based designed inhibitors remain a powerful alternative, which can be tailor-made limiting the potential impact of viral escape mutations. Our work harnesses this approach to build designer inhibitors of orders of magnitude higher affinity and demonstrating complete recognition of the antigen's epitopes.

DATA AND SOFTWARE AVAILABILITY

Initial coordinates of the proteins are taken form protein data bank (https://www.rcsb.org/downloads). Mutation of residues and fixing of missing residues and atoms are carried out with "pdbfixer" tools (https://github.com/openmm/pdbfixer). Amino acids of the proteins were protonated by the H++ server (http://biophysics.cs.vt.edu/hppdetails.php). The peptide structure is generated using chimera software (https://www.cgl.ucsf.edu/chimera/download.html). The MD simulations reported in this study are performed using Gromacs 4.5.5 software (ftp://ftp.gromacs.org/pub/gromacs/gromacs-4.5.5.tar.gz). The Gromacs's tools employed for data analysis (e.g., *g_mindist*, *g_hbond*, *g_rms*, and *g_energy*) are implemented in the 4.5.5 version (https://manual.gromacs.org/archive/4.5/online.html). Docking and metadynamics simulations are performed by implementing PLUMED-1.3 (https://www.plumed.org/pdf/manual_1-3-0.pdf) patch to the gromacs-4.5.5 software Structures, visualization and image rendering was carried out using VMD-1.9.1 (https://www.ks.uiuc.edu/Research/vmd/vmd-1.9.1/) (see the Methods section for further details).

ASSOCIATED CONTENT

Supporting Information. vdW contacts between residues of SARS-COV-2 RBD with hACE2, and its inhibitors (Fab, mFab, nanobody and designer peptide), characterization of the RBD-hACE2 and RBD-inhibitors' binding basins, compositions of the simulating systems, RMSD of the backbone atoms of the inhibitors, and convergence of the metadynamics simulations (PDF)

AUTHOR INFORMATION

Corresponding Author

* btusar@barc.gov.in

Notes

The authors declare no competing financial interest.

ACKNOWLEDGMENT

The authors thank computer centre, BARC for providing the ANUPAM parallel computational facility. The work was supported by DAE under project XII-N-R&D-02.04/Theoretical & Computational Chemistry of Complex Systems.

REFERENCES

1. Chan, J. F.-W.; Yuan, S.; Kok, K.-H.; To, K. K.-W.; Chu, H.; Yang, J.; Xing, F.; Liu, J.; Yip, C. C.-Y.; Poon, R. W.-S.; Tsoi, H.-W.; Lo, S. K.-F.; Chan, K.-H.; Poon, V. K.-M.; Chan, W.-M.; Ip, J. D.; Cai, J.-P.; Cheng, V. C.-C.; Chen, H.; Hui, C. K.-M.; Yuen, K.-Y., A familial cluster of pneumonia associated with the 2019 novel coronavirus indicating person-to-person transmission: a study of a family cluster. *The Lancet* **2020,** *395* (10223), 514-523.
2. McKee, M.; Stuckler, D., If the world fails to protect the economy, COVID-19 will damage health not just now but also in the future. *Nature Medicine* **2020,** *26* (5), 640-642.
3. Houriiyah, T.; Eduan, W.; Marta, G.; Arash, I.; Vagner, F.; Jennifer, G.; Deelan, D.; Sureshnee, P.; Emmanuel James, S.; Nokukhanya, M.; Koleka, M.; Anne von, G.; Sibongile, W.; Mushal, A.; Arshad, I.; Thabo, M.; Allison, J. G.; Susan, E.; Gert Van, Z.; Wolfgang, P.; Francesco, P.; Alex, S.; Diana, H.; Gert, M.; Marvin, H.; Stephen, K.; Mary-Ann, D.; Lynn, T.; Innocent, M.; Denis, Y.; Caroline, M.; Dominique, G.; Shareef, A.; Oluwakemi, L.-A.; Arghavan, A.-D.; Adam, G.; Constantinos Kurt, W.; Bryan Trevor, S.; José, L.; Luiz Carlos Junior, A.; Sergei, L. K. P.; Steven, W.; Darren, M.; Richard, J. L.; Jinal, N. B.; Carolyn, W.; Tulio de, O., Detection of a SARS-CoV-2 variant of concern in South Africa. *Nature 592* (1476-4687), 438-443.
4. Zaki, A. M.; van Boheemen, S.; Bestebroer, T. M.; Osterhaus, A. D. M. E.; Fouchier, R. A. M., Isolation of a Novel Coronavirus from a Man with Pneumonia in Saudi Arabia. *New England Journal of Medicine* **2012,** *367* (19), 1814-1820.
5. Constantinos Kurt, W.; Frances, A.; Tandile, H.; Mashudu, M.; Prudence, K.; Brent, O.; Bronwen, E. L.; Tulio de, O.; Marion, V.; Karin van der, B.; Theresa, R.; Michael, B.; Veronica, U.; Susan, M.; Anne von, G.; Cheryl, C.; Lynn, M.; Jinal, N. B.; Penny, L. M., SARS-CoV-2 501Y.V2 escapes neutralization by South African COVID-19 donor plasma. *Nature medicine* (1546-170X).
6. Arya, R.; Kumari, S.; Pandey, B.; Mistry, H.; Bihani, S. C.; Das, A.; Prashar, V.; Gupta, G. D.; Panicker, L.; Kumar, M., Structural insights into SARS-CoV-2 proteins. *Journal of Molecular Biology* **2021,** *433* (2), 166725.
7. Lu, R.; Zhao, X.; Li, J.; Niu, P.; Yang, B.; Wu, H.; Wang, W.; Song, H.; Huang, B.; Zhu, N.; Bi, Y.; Ma, X.; Zhan, F.; Wang, L.; Hu, T.; Zhou, H.; Hu, Z.; Zhou, W.; Zhao, L.; Chen, J.; Meng, Y.; Wang, J.; Lin, Y.; Yuan, J.; Xie, Z.; Ma, J.; Liu, W. J.; Wang, D.; Xu, W.; Holmes, E. C.; Gao, G. F.; Wu, G.; Chen, W.; Shi, W.; Tan, W., Genomic characterisation and epidemiology of 2019 novel coronavirus: implications for virus origins and receptor binding. *The Lancet* **2020,** *395* (10224), 565-574.
8. Ali, A.; Vijayan, R., Dynamics of the ACE2–SARS-CoV-2/SARS-CoV spike protein interface reveal unique mechanisms. *Scientific Reports* **2020,** *10* (1), 14214.
9. Bai, C.; Warshel, A., Critical Differences between the Binding Features of the Spike Proteins of SARS-CoV-2 and SARS-CoV. *The Journal of Physical Chemistry B* **2020,** *124* (28), 5907-5912.
10. García-Iriepa, C.; Hognon, C.; Francés-Monerris, A.; Iriepa, I.; Miclot, T.; Barone, G.; Monari, A.; Marazzi, M., Thermodynamics of the Interaction between the Spike Protein of Severe Acute Respiratory Syndrome Coronavirus-2 and the Receptor of Human Angiotensin-Converting Enzyme 2. Effects of Possible Ligands. *The Journal of Physical Chemistry Letters* **2020,** *11* (21), 9272-9281.

11. Ghorbani, M.; Brooks, B. R.; Klauda, J. B., Critical Sequence Hotspots for Binding of Novel Coronavirus to Angiotensin Converter Enzyme as Evaluated by Molecular Simulations. *The Journal of Physical Chemistry B* **2020,** *124* (45), 10034-10047.
12. Lan, J.; Ge, J.; Yu, J.; Shan, S.; Zhou, H.; Fan, S.; Zhang, Q.; Shi, X.; Wang, Q.; Zhang, L.; Wang, X., Structure of the SARS-CoV-2 spike receptor-binding domain bound to the ACE2 receptor. *Nature* **2020,** *581* (7807), 215-220.
13. Laurini, E.; Marson, D.; Aulic, S.; Fermeglia, M.; Pricl, S., Computational Alanine Scanning and Structural Analysis of the SARS-CoV-2 Spike Protein/Angiotensin-Converting Enzyme 2 Complex. *ACS Nano* **2020,** *14* (9), 11821-11830.
14. Moreira, R. A.; Chwastyk, M.; Baker, J. L.; Guzman, H. V.; Poma, A. B., Quantitative determination of mechanical stability in the novel coronavirus spike protein. *Nanoscale* **2020,** *12* (31), 16409-16413.
15. Nguyen, H. L.; Lan, P. D.; Thai, N. Q.; Nissley, D. A.; O'Brien, E. P.; Li, M. S., Does SARS-CoV-2 Bind to Human ACE2 More Strongly Than Does SARS-CoV? *The Journal of Physical Chemistry B* **2020,** *124* (34), 7336-7347.
16. Peng, C.; Zhu, Z.; Shi, Y.; Wang, X.; Mu, K.; Yang, Y.; Zhang, X.; Xu, Z.; Zhu, W., Computational Insights into the Conformational Accessibility and Binding Strength of SARS-CoV-2 Spike Protein to Human Angiotensin-Converting Enzyme 2. *The Journal of Physical Chemistry Letters* **2020,** *11* (24), 10482-10488.
17. Qiao, B.; Olvera de la Cruz, M., Enhanced Binding of SARS-CoV-2 Spike Protein to Receptor by Distal Polybasic Cleavage Sites. *ACS Nano* **2020,** *14* (8), 10616-10623.
18. Serapian, S. A.; Marchetti, F.; Triveri, A.; Morra, G.; Meli, M.; Moroni, E.; Sautto, G. A.; Rasola, A.; Colombo, G., The Answer Lies in the Energy: How Simple Atomistic Molecular Dynamics Simulations May Hold the Key to Epitope Prediction on the Fully Glycosylated SARS-CoV-2 Spike Protein. *The Journal of Physical Chemistry Letters* **2020,** *11* (19), 8084-8093.
19. Shang, J.; Wan, Y.; Luo, C.; Ye, G.; Geng, Q.; Auerbach, A.; Li, F., Cell entry mechanisms of SARS-CoV-2. *Proceedings of the National Academy of Sciences* **2020,** *117* (21), 11727.
20. Silva de Souza, A.; Rivera, J. D.; Almeida, V. M.; Ge, P.; de Souza, R. F.; Farah, C. S.; Ulrich, H.; Marana, S. R.; Salinas, R. K.; Guzzo, C. R., Molecular Dynamics Reveals Complex Compensatory Effects of Ionic Strength on the Severe Acute Respiratory Syndrome Coronavirus 2 Spike/Human Angiotensin-Converting Enzyme 2 Interaction. *The Journal of Physical Chemistry Letters* **2020,** *11* (24), 10446-10453.
21. Spinello, A.; Saltalamacchia, A.; Magistrato, A., Is the Rigidity of SARS-CoV-2 Spike Receptor-Binding Motif the Hallmark for Its Enhanced Infectivity? Insights from All-Atom Simulations. *The Journal of Physical Chemistry Letters* **2020,** *11* (12), 4785-4790.
22. Wang, Q.; Zhang, Y.; Wu, L.; Niu, S.; Song, C.; Zhang, Z.; Lu, G.; Qiao, C.; Hu, Y.; Yuen, K.-Y.; Wang, Q.; Zhou, H.; Yan, J.; Qi, J., Structural and Functional Basis of SARS-CoV-2 Entry by Using Human ACE2. *Cell* **2020,** *181* (4), 894-904.
23. Wang, Y.; Liu, M.; Gao, J., Enhanced receptor binding of SARS-CoV-2 through networks of hydrogen-bonding and hydrophobic interactions. *Proceedings of the National Academy of Sciences* **2020,** *117* (25), 13967.
24. Yan, R.; Zhang, Y.; Li, Y.; Xia, L.; Guo, Y.; Zhou, Q., Structural basis for the recognition of SARS-CoV-2 by full-length human ACE2. *Science* **2020,** *367* (6485), 1444-14448.
25. Yang, J.; Petitjean, S. J. L.; Koehler, M.; Zhang, Q.; Dumitru, A. C.; Chen, W.; Derclaye, S.; Vincent, S. P.; Soumillion, P.; Alsteens, D., Molecular interaction and inhibition of SARS-CoV-2 binding to the ACE2 receptor. *Nature Communications* **2020,** *11* (1), 4541.

26. Laurini, E.; Marson, D.; Aulic, S.; Fermeglia, A.; Pricl, S., Computational Mutagenesis at the SARS-CoV-2 Spike Protein/Angiotensin-Converting Enzyme 2 Binding Interface: Comparison with Experimental Evidence. *ACS Nano* **2021**.
27. Donoghue, M.; Wakimoto, H.; Maguire, C. T.; Acton, S.; Hales, P.; Stagliano, N.; Fairchild-Huntress, V.; Xu, J.; Lorenz, J. N.; Kadambi, V.; Berul, C. I.; Breitbart, R. E., Heart block, ventricular tachycardia, and sudden death in ACE2 transgenic mice with downregulated connexins. *Journal of Molecular and Cellular Cardiology* **2003,** *35* (9), 1043-1053.
28. Walls, A. C.; Park, Y.-J.; Tortorici, M. A.; Wall, A.; McGuire, A. T.; Veesler, D., Structure, Function, and Antigenicity of the SARS-CoV-2 Spike Glycoprotein. *Cell* **2020,** *181* (2), 281-292.e6.
29. Wrapp, D.; Wang, N.; Corbett, K. S.; Goldsmith, J. A.; Hsieh, C.-L.; Abiona, O.; Graham, B. S.; McLellan, J. S., Cryo-EM structure of the 2019-nCoV spike in the prefusion conformation. *Science* **2020,** *367* (6483), 1260.
30. Casalino, L.; Gaieb, Z.; Goldsmith, J. A.; Hjorth, C. K.; Dommer, A. C.; Harbison, A. M.; Fogarty, C. A.; Barros, E. P.; Taylor, B. C.; McLellan, J. S.; Fadda, E.; Amaro, R. E., Beyond Shielding: The Roles of Glycans in the SARS-CoV-2 Spike Protein. *ACS Central Science* **2020,** *6* (10), 1722-1734.
31. Chen, Q.; Allot, A.; Lu, Z., LitCovid: an open database of COVID-19 literature. *Nucleic Acids Research* **2021,** *49* (D1), D1534-D1540.
32. Xiu, S.; Dick, A.; Ju, H.; Mirzaie, S.; Abdi, F.; Cocklin, S.; Zhan, P.; Liu, X., Inhibitors of SARS-CoV-2 Entry: Current and Future Opportunities. *Journal of Medicinal Chemistry* **2020,** *63* (21), 12256-12274.
33. Zou, J.; Yin, J.; Fang, L.; Yang, M.; Wang, T.; Wu, W.; Bellucci, M. A.; Zhang, P., Computational Prediction of Mutational Effects on SARS-CoV-2 Binding by Relative Free Energy Calculations. *Journal of Chemical Information and Modeling* **2020**.
34. Zhang, Y.; Kutateladze, T. G., Molecular structure analyses suggest strategies to therapeutically target SARS-CoV-2. *Nature Communications* **2020,** *11* (1), 2920.
35. Chowdhury, S. M.; Talukder, S. A.; Khan, A. M.; Afrin, N.; Ali, M. A.; Islam, R.; Parves, R.; Al Mamun, A.; Sufian, M. A.; Hossain, M. N.; Hossain, M. A.; Halim, M. A., Antiviral Peptides as Promising Therapeutics against SARS-CoV-2. *The Journal of Physical Chemistry B* **2020,** *124* (44), 9785-9792.
36. Sitthiyotha, T.; Chunsrivirot, S., Computational Design of 25-mer Peptide Binders of SARS-CoV-2. *The Journal of Physical Chemistry B* **2020,** *124* (48), 10930-10942.
37. Han, Y.; Král, P., Computational Design of ACE2-Based Peptide Inhibitors of SARS-CoV-2. *ACS Nano* **2020,** *14* (4), 5143-5147.
38. Glasgow, A.; Glasgow, J.; Limonta, D.; Solomon, P.; Lui, I.; Zhang, Y.; Nix, M. A.; Rettko, N. J.; Zha, S.; Yamin, R.; Kao, K.; Rosenberg, O. S.; Ravetch, J. V.; Wiita, A. P.; Leung, K. K.; Lim, S. A.; Zhou, X. X.; Hobman, T. C.; Kortemme, T.; Wells, J. A., Engineered ACE2 receptor traps potently neutralize SARS-CoV-2. *Proceedings of the National Academy of Sciences* **2020,** *117* (45), 28046.
39. Ling, R.; Dai, Y.; Huang, B.; Huang, W.; Yu, J.; Lu, X.; Jiang, Y., In silico design of antiviral peptides targeting the spike protein of SARS-CoV-2. *Peptides* **2020,** *130*, 170328.
40. DeFrancesco, L., COVID-19 antibodies on trial. *Nature Biotechnology* **2020,** *38* (11), 1242-1252.
41. Duan, K.; Liu, B.; Li, C.; Zhang, H.; Yu, T.; Qu, J.; Zhou, M.; Chen, L.; Meng, S.; Hu, Y.; Peng, C.; Yuan, M.; Huang, J.; Wang, Z.; Yu, J.; Gao, X.; Wang, D.; Yu, X.; Li, L.; Zhang, J.;

Wu, X.; Li, B.; Xu, Y.; Chen, W.; Peng, Y.; Hu, Y.; Lin, L.; Liu, X.; Huang, S.; Zhou, Z.; Zhang, L.; Wang, Y.; Zhang, Z.; Deng, K.; Xia, Z.; Gong, Q.; Zhang, W.; Zheng, X.; Liu, Y.; Yang, H.; Zhou, D.; Yu, D.; Hou, J.; Shi, Z.; Chen, S.; Chen, Z.; Zhang, X.; Yang, X., Effectiveness of convalescent plasma therapy in severe COVID-19 patients. *Proceedings of the National Academy of Sciences* **2020,** *117* (17), 9490.
42. Ju, B.; Zhang, Q.; Ge, J.; Wang, R.; Sun, J.; Ge, X.; Yu, J.; Shan, S.; Zhou, B.; Song, S.; Tang, X.; Yu, J.; Lan, J.; Yuan, J.; Wang, H.; Zhao, J.; Zhang, S.; Wang, Y.; Shi, X.; Liu, L.; Zhao, J.; Wang, X.; Zhang, Z.; Zhang, L., Human neutralizing antibodies elicited by SARS-CoV-2 infection. *Nature* **2020,** *584* (7819), 115-119.
43. Shi, R.; Shan, C.; Duan, X.; Chen, Z.; Liu, P.; Song, J.; Song, T.; Bi, X.; Han, C.; Wu, L.; Gao, G.; Hu, X.; Zhang, Y.; Tong, Z.; Huang, W.; Liu, W. J.; Wu, G.; Zhang, B.; Wang, L.; Qi, J.; Feng, H.; Wang, F.-S.; Wang, Q.; Gao, G. F.; Yuan, Z.; Yan, J., A human neutralizing antibody targets the receptor-binding site of SARS-CoV-2. *Nature* **2020,** *584* (7819), 120-124.
44. Garber, K., Hunt for improved monoclonals against coronavirus gathers pace. *Nature Biotechnology* **2021,** *39* (1), 9-12.
45. Luan, B.; Huynh, T., In Silico Antibody Mutagenesis for Optimizing Its Binding to Spike Protein of Severe Acute Respiratory Syndrome Coronavirus 2. *The Journal of Physical Chemistry Letters* **2020,** *11* (22), 9781-9787.
46. Jiang, S.; Zhang, X.; Yang, Y.; Hotez, P. J.; Du, L., Neutralizing antibodies for the treatment of COVID-19. *Nature Biomedical Engineering* **2020,** *4* (12), 1134-1139.
47. Wu, Y.; Wang, F.; Shen, C.; Peng, W.; Li, D.; Zhao, C.; Li, Z.; Li, S.; Bi, Y.; Yang, Y.; Gong, Y.; Xiao, H.; Fan, Z.; Tan, S.; Wu, G.; Tan, W.; Lu, X.; Fan, C.; Wang, Q.; Liu, Y.; Zhang, C.; Qi, J.; Gao, G. F.; Gao, F.; Liu, L., A noncompeting pair of human neutralizing antibodies block COVID-19 virus binding to its receptor ACE2. *Science* **2020,** *368* (6496), 1274.
48. Chen, R. E.; Zhang, X.; Case, J. B.; Winkler, E. S.; Liu, Y.; VanBlargan, L. A.; Liu, J.; Errico, J. M.; Xie, X.; Suryadevara, N.; Gilchuk, P.; Zost, S. J.; Tahan, S.; Droit, L.; Turner, J. S.; Kim, W.; Schmitz, A. J.; Thapa, M.; Wang, D.; Boon, A. C. M.; Presti, R. M.; O'Halloran, J. A.; Kim, A. H. J.; Deepak, P.; Pinto, D.; Fremont, D. H.; Crowe, J. E.; Corti, D.; Virgin, H. W.; Ellebedy, A. H.; Shi, P.-Y.; Diamond, M. S., Resistance of SARS-CoV-2 variants to neutralization by monoclonal and serum-derived polyclonal antibodies. *Nature Medicine* **2021**.
49. Tortorici, M. A.; Beltramello, M.; Lempp, F. A.; Pinto, D.; Dang, H. V.; Rosen, L. E.; McCallum, M.; Bowen, J.; Minola, A.; Jaconi, S.; Zatta, F.; De Marco, A.; Guarino, B.; Bianchi, S.; Lauron, E. J.; Tucker, H.; Zhou, J.; Peter, A.; Havenar-Daughton, C.; Wojcechowskyj, J. A.; Case, J. B.; Chen, R. E.; Kaiser, H.; Montiel-Ruiz, M.; Meury, M.; Czudnochowski, N.; Spreafico, R.; Dillen, J.; Ng, C.; Sprugasci, N.; Culap, K.; Benigni, F.; Abdelnabi, R.; Foo, S.-Y. C.; Schmid, M. A.; Cameroni, E.; Riva, A.; Gabrieli, A.; Galli, M.; Pizzuto, M. S.; Neyts, J.; Diamond, M. S.; Virgin, H. W.; Snell, G.; Corti, D.; Fink, K.; Veesler, D., Ultrapotent human antibodies protect against SARS-CoV-2 challenge via multiple mechanisms. *Science* **2020,** *370* (6519), 950-957.
50. Hanke, L.; Vidakovics Perez, L.; Sheward, D. J.; Das, H.; Schulte, T.; Moliner-Morro, A.; Corcoran, M.; Achour, A.; Karlsson Hedestam, G. B.; Hällberg, B. M.; Murrell, B.; McInerney, G. M., An alpaca nanobody neutralizes SARS-CoV-2 by blocking receptor interaction. *Nature Communications* **2020,** *11* (1), 4420.
51. Forni, G.; Mantovani, A.; Forni, G.; Mantovani, A.; Moretta, L.; Rappuoli, R.; Rezza, G.; Bagnasco, A.; Barsacchi, G.; Bussolati, G.; Cacciari, M.; Cappuccinelli, P.; Cheli, E.; Guarini, R.; Bacci, M. L.; Mancini, M.; Marcuzzo, C.; Morrone, M. C.; Parisi, G.; Pasquino, G.; Patrono, C.; Curzio, A. Q.; Remuzzi, G.; Roncaglia, A.; Schiaffino, S.; Vineis, P.; on behalf of the Covid-19

Commission of Accademia Nazionale dei Lincei, R., COVID-19 vaccines: where we stand and challenges ahead. *Cell Death & Differentiation* **2021,** *28* (2), 626-639.
52. Li, Y.; Wan, Y.; Liu, P.; Zhao, J.; Lu, G.; Qi, J.; Wang, Q.; Lu, X.; Wu, Y.; Liu, W.; Zhang, B.; Yuen, K.-Y.; Perlman, S.; Gao, G. F.; Yan, J., A humanized neutralizing antibody against MERS-CoV targeting the receptor-binding domain of the spike protein. *Cell Research* **2015,** *25* (11), 1237-1249.
53. Du, L.; He, Y.; Zhou, Y.; Liu, S.; Zheng, B.-J.; Jiang, S., The spike protein of SARS-CoV — a target for vaccine and therapeutic development. *Nature Reviews Microbiology* **2009,** *7* (3), 226-236.
54. Wang, D.; Ge, Y.; Zhong, B.; Liu, D., Specific epitopes form extensive hydrogen-bonding networks to ensure efficient antibody binding of SARS-CoV-2: Implications for advanced antibody design. *Computational and Structural Biotechnology Journal* **2021,** *19*, 1661-1671.
55. Cao, Y.; Su, B.; Guo, X.; Sun, W.; Deng, Y.; Bao, L.; Zhu, Q.; Zhang, X.; Zheng, Y.; Geng, C.; Chai, X.; He, R.; Li, X.; Lv, Q.; Zhu, H.; Deng, W.; Xu, Y.; Wang, Y.; Qiao, L.; Tan, Y.; Song, L.; Wang, G.; Du, X.; Gao, N.; Liu, J.; Xiao, J.; Su, X.-d.; Du, Z.; Feng, Y.; Qin, C.; Qin, C.; Jin, R.; Xie, X. S., Potent Neutralizing Antibodies against SARS-CoV-2 Identified by High-Throughput Single-Cell Sequencing of Convalescent Patients' B Cells. *Cell* **2020,** *182* (1), 73-84.
56. Leader, B.; Baca, Q. J.; Golan, D. E., Protein therapeutics: a summary and pharmacological classification. *Nature Reviews Drug Discovery* **2008,** *7* (1), 21-39.
57. Bodier-Montagutelli, E.; Mayor, A.; Vecellio, L.; Respaud, R.; Heuzé-Vourc'h, N., Designing inhaled protein therapeutics for topical lung delivery: what are the next steps? *Expert Opinion on Drug Delivery* **2018,** *15* (8), 729-736.
58. Jianliang, X.; Kai, X.; Seolkyoung, J.; Andrea, C.; Jenna, L.; Frauke, M.; Julio Cesar Cetrulo, L.; Solji, P.; Fabian, S.; Zijun, W.; Yaoxing, H.; Yang, L.; Manoj, N.; Pengfei, W.; Jonathan, E. S.; Lino, T.; Tatsiana, B.; Gwo-Yu, C.; Adam, S. O.; Tyler, S.; Teng, I. T.; Yaroslav, T.; Tongqing, Z.; Vincent, M.; David, D. H.; Theodora, H.; Paul, D. B.; Michel, C. N.; Peter, D. K.; Rafael, C., Nanobodies from camelid mice and llamas neutralize SARS-CoV-2 variants. *Nature* (1476-4687).
59. Barducci, A.; Bussi, G.; Parrinello, M., Well-Tempered Metadynamics: A Smoothly Converging and Tunable Free-Energy Method. *Physical Review Letters* **2008,** *100* (2), 020603.
60. Eastman, P.; Swails, J.; Chodera, J. D.; McGibbon, R. T.; Zhao, Y.; Beauchamp, K. A.; Wang, L.-P.; Simmonett, A. C.; Harrigan, M. P.; Stern, C. D.; Wiewiora, R. P.; Brooks, B. R.; Pande, V. S., OpenMM 7: Rapid development of high performance algorithms for molecular dynamics. *PLOS Computational Biology* **2017,** *13* (7), e1005659.
61. Anandakrishnan, R.; Aguilar, B.; Onufriev, A. V., H++ 3.0: automating pK prediction and the preparation of biomolecular structures for atomistic molecular modeling and simulations. *Nucleic Acids Research* **2012,** *40* (W1), W537-W541.
62. Pronk, S.; Páll, S.; Schulz, R.; Larsson, P.; Bjelkmar, P.; Apostolov, R.; Shirts, M. R.; Smith, J. C.; Kasson, P. M.; van der Spoel, D.; Hess, B.; Lindahl, E., GROMACS 4.5: a high-throughput and highly parallel open source molecular simulation toolkit. *Bioinformatics* **2013,** *29* (7), 845-854.
63. Lindorff-Larsen, K.; Piana, S.; Palmo, K.; Maragakis, P.; Klepeis, J. L.; Dror, R. O.; Shaw, D. E., Improved side-chain torsion potentials for the Amber ff99SB protein force field. *Proteins: Structure, Function, and Bioinformatics* **2010,** *78* (8), 1950-1958.

64. Jorgensen, W. L.; Jenson, C., Temperature dependence of TIP3P, SPC, and TIP4P water from NPT Monte Carlo simulations: Seeking temperatures of maximum density. *Journal of Computational Chemistry* **1998,** *19* (10), 1179-1186.
65. Hess, B.; Bekker, H.; Berendsen Herman, J. C.; Fraaije Johannes, G. E. M., LINCS: A linear constraint solver for molecular simulations. *Journal of Computational Chemistry* **1998,** *18* (12), 1463-1472.
66. Berendsen, H. J. C.; Postma, J. P. M.; van Gunsteren, W. F.; DiNola, A.; Haak, J. R., Molecular dynamics with coupling to an external bath. *The Journal of Chemical Physics* **1984,** *81* (8), 3684-3690.
67. Bussi, G.; Donadio, D.; Parrinello, M., Canonical sampling through velocity rescaling. *The Journal of Chemical Physics* **2007,** *126* (1), 014101.
68. Darden, T.; York, D.; Pedersen, L., Particle mesh Ewald: An N·log(N) method for Ewald sums in large systems. *The Journal of Chemical Physics* **1993,** *98* (12), 10089-10092.
69. Essmann, U.; Perera, L.; Berkowitz, M. L.; Darden, T.; Lee, H.; Pedersen, L. G., A smooth particle mesh Ewald method. *The Journal of Chemical Physics* **1995,** *103* (19), 8577-8593.
70. Pettersen, E. F.; Goddard, T. D.; Huang, C. C.; Couch, G. S.; Greenblatt, D. M.; Meng, E. C.; Ferrin, T. E., UCSF Chimera—A visualization system for exploratory research and analysis. *Journal of Computational Chemistry* **2004,** *25* (13), 1605-1612.
71. Gervasio, F. L.; Laio, A.; Parrinello, M., Flexible Docking in Solution Using Metadynamics. *Journal of the American Chemical Society* **2005,** *127* (8), 2600-2607.
72. Bonomi, M.; Branduardi, D.; Bussi, G.; Camilloni, C.; Provasi, D.; Raiteri, P.; Donadio, D.; Marinelli, F.; Pietrucci, F.; Broglia, R. A.; Parrinello, M., PLUMED: A portable plugin for free-energy calculations with molecular dynamics. *Computer Physics Communications* **2009,** *180* (10), 1961-1972.
73. Wall, E. C.; Wu, M.; Harvey, R.; Kelly, G.; Warchal, S.; Sawyer, C.; Daniels, R.; Hobson, P.; Hatipoglu, E.; Ngai, Y.; Hussain, S.; Nicod, J.; Goldstone, R.; Ambrose, K.; Hindmarsh, S.; Beale, R.; Riddell, A.; Gamblin, S.; Howell, M.; Kassiotis, G.; Libri, V.; Williams, B.; Swanton, C.; Gandhi, S.; Bauer, D. L. V., Neutralising antibody activity against SARS-CoV-2 VOCs B.1.617.2 and B.1.351 by BNT162b2 vaccination. *The Lancet 10.1016/S0140-6736(21)01290-3*.
74. Khan, A.; Zia, T.; Suleman, M.; Khan, T.; Ali, S. S.; Abbasi, A. A.; Mohammad, A.; Wei, D.-Q., Higher infectivity of the SARS-CoV-2 new variants is associated with K417N/T, E484K, and N501Y mutants: An insight from structural data. *Journal of Cellular Physiology*, 1-13. https://doi.org/10.1002/jcp.30367.

Table 1. SARS-COV-2 S/RBD binding to hACE2. The first number in the parentheses represents the vdw contacts, while the second number is for potential hydrogen bonds the indicated residues of hACE2 conferred with S/RBD (first column). For a complete list of vdw interacting residues see supporting information, Table S1. Shading of the rows indicates the RBD-hACE2 contact regions (light green: CR1; orange: CR2; yellow: CR3).

SARS-COV-2 S/RBD	hACE2
R403	H34(6,1), E37(3,1)
K417	D30(3,2), H34(3,1)
G446	Q42(7,1)
G447	Q42(7,1)
Y449	D38(2,2), Q42(5,1)
Y453	H34(10,2)
A475	S19(7,2), Q24(4,1)
G476	S19(9,3), Q24(7,1)
S477	S19(8,1), Q24(6,3)
N487	Q24(7,3), Y83(2,3)
Q493	K31(3,2), H34(3,1), E35(6,2)
G496	D38(2,1),K353(4,1)
Q498	D38(1,1), Y41(5,1), Q42(8,3)
T500	Y41(3,2), N330(2,1), D355(2,1), R357(2,1)
N501	Y41(10,1), K353(11,3), D355(2,1)
G502	K353(1,1), D355(1,1)
Y505	E37(2,2), R393(3,2)

Table 2. Comparison of SARS-COV-2 S/RBD binding to the antibody, B38, and its mutant. The first number in the parentheses of the ligands represents the vdw contacts, while the second number is for potential H-bonds the indicated residues conferred with S/RBD (first column). For a complete list of vdw interacting residues see supporting information, Tables S1 and S2. Shading of the rows (light green: CR1; Orange: CR2; Yellow: CR3) corresponds to the RBD-hACE2 contact regions (*cf.* Table 1). The reported CDRs of B38 is indicated.[47] Residues coloured in blue and red represent those from the heavy and the light chain of the antibody, respectively.

SARS-COV-2 S/RBD	B38	Mutated B38
R403	Y32(2,1), N92(7,4) (*LCDR1, 2*)	Y32(2,1), N92(6,4) (*LCDR1, 2*)
D405	D0(6,1)	D0(4,1)
E406	Y32(2,1), N92(4,1) (*LCDR1, 2*)	N92(4,2) (*LCDR2*)
R408	D0(5,4), Y94(14,2) (*LCDR2*)	Y58(5,2) (*HCDR2*) D0(5,3), Y94(14,2) (*LCDR2*)
T415	Y58(4,2) (*HCDR2*)	T57(1,1), Y58(4,2) (*HCDR2*)
K417	Y33(5,1), Y52(5,1) (*HCDR2*), E98(2,2) N92(6,2) (*LCDR2*), Y97(3,1)	Y33(5,1), Y52(6,1), E98(3,2) (*HCDR2*) N92(7,2), Y97(3, 1) (*LCDR2*)
D420	S56(2,2)	S56(3,2)
Y421	Y33(3,1), S53(4,1), G54(1,1)	S53(3,1), G54(5,2), G55(1,1), S56(3,2)
G446		S67(6,1)
Y449	S31(4,1)	S31(4,1)
Y453	Y32(3,1), N92(2,1) (*LCDR1, 2*)	Y32(3,1), N92(6,2) (*LCDR1, 2*)
L455	Y33(2,1)	Y33(1,1)
R457	S53(3,2)	S53(4,2)
K458	S30(6,2), S31(4,2) (*HCDR1*)	S30(6,2), S31(4,1) (*HCDR1*)
N460	G54(4,1),G55(3,1), S56(2,1)	G54(3,2), G55(5,3), S56(4,3)
Y473	S31(4,2) (*HCDR1*)	S31(3,1), S53(1,1) (*HCDR1*)
Q474	S31(3,1) (*HCDR*)	S31(4,1) (*HCDR1*)
A475	I28(3,1), N32(2,1) (*HCDR1*)	128(6,1), S31(6,1), N32(4,1) (*HCDR1*)
G476		Q27(5,1)
S477	D0(4,4), G26(2,2 (*HCDR1*)	Q27(6,4)
T478	D0(7,4)	Q27(6,3)
E484	Y100(3,2) (*HCDR3*)	Y100(7,2) (*HCDR3*)
F486		D0(10,2)
N487	D0(4,3), G26(1,1),R97(2,2) (*HCDR1, 3*)	G26(2,1), Q27(7,2), I28(3,1), N32(1,1), R97(3,4) (*HCDR1, 3*)
Y489	R97(9,2), D103(2,2) (*HCDR3*)	N32(2,1), R97(5,2) (*HCDR1*)
F490	Y100(3,2) (*HCDR3*)	Y100(3,2) (*HCDR3*)
Q493	Y32(7,1) (*LCDR1*)	Y100(9,2) (*HCDR3*) Y32(7 ,2), N92(4,2) (*LCDR1, 2*)
S494	S31(3,1), Y32(4,1) (*LCDR1*)	Y32(5,1) (*LCDR1*)
Y495	S30(2,1), S31(2,1) (*LCDR1*)	S30(3,1), S31(1,1), Y32(3,1) (*LCDR1*)
G496	S30(4,1) (*LCDR1*)	S30(4,1) (*LCDR1*)
Q498	S30(5,3) (*LCDR1*), S67(3,1)	S30(4,4), S31(2,1), S67(9,3), G68(5,1) (*LCDR1*)
T500	Q27(7 ,1), S67(2,1), T69(4,1)	Q27(5,1), G28(3,1), G68(1,1), T69(5,1)
N501	Q27(2), S30(4,4) (*LCDR1*)	Q27(2,1), G28(2,1), I29(1,1), S30(4,4) (*LCDR1*)
G502	G28(5,2)	G28(6,2)
V503	D0(7,1), Q27(7,1)	
G504	D0(7,1)	D0(6,2)
Y505	Q90(2,1), L91(1,1), N92(2,1) (*LCDR2*)	Q90(2,1), L91(1,1), N92(2,1) (*LCDR2*)

Table 3. Comparison of SARS-COV-2 S/RBD binding to nanobody, Ty1 and Ty1-based peptide. The first number in the parentheses of the ligands represents the vdw contacts, while the second number is for potential H-bonds the indicated residues conferred with S/RBD (first column). For a complete list of vdw interacting residues see supporting information, Tables S1 and S2 Shading of the rows (light green: CR1; Orange: CR2; Yellow: CR3) correspond to the RBD-hACE2 contact regions (*cf.* Table 1). The reported CDRs of Ty1 is indicated.[50]

SARS-COV-2 S/RBD	Ty1	Ty1-based peptide
R346	Q3(2,2)	
R349	Q3(5,4)	
Y351	Q3(2,2),V4(6,1)	
R403		G111(4,2), Q112(7,9)
R408		S33(6,4)
T415		Q3(7,1), G44(2,1), K45(3,1)
K417		Y35(14,3), G46(1,1), P47(1,1), E48(4,2), Q112(6,4)
D420		Q3(2,2), G44(1,1)
Y421		G44(5,1), K45(7,2), G46(1,1)
K444	Q112(4,3)	
V445	Q112(2,1)	
G446	R110(10,1), Q112(3,1)	S105(5,1), R110(10,2)
G447	Q112(3,1)	S105(4,1)
N448	Q112(3,1)	
Y449	R110(13,3), Q112(3,2)	N56(1,1), N103(8,2), S105(6,3), S108(4,1), R110(13,2)
N450	Q3(9,5), V4(1,1), Q5(10,4), L6(2,1), Q112(6,4)	N103(4,1), S105(3,1)
Y453		G111(4,2), Q112(2,1)
K458		Q3(8,2), Q5(8,2)
N460		Q3(5,1), G44(2,1), K45(10,1)
T470	G28(1,1), T30(3,2) (*CDR1*)	
Y473		Q3(5,1), Q5(6,2)
Q474		Q3(11,5)
A475		Q3(7,2)
G476		Q3(11,2)
S477		Q3(11,2)
T478		
G482	S32(4,1), S33(5,1) (*CDR1*)	
E484	S32(1,1), S33(4,1), Y35(2,1), N56(1,1), N103(4,3) (*CDR1, 2, 3*)	
G485	N103(4,3) (*CDR3*)	
F486	N103(7,1) (*CDR3*)	
N487	N103(8,2) (*CDR3*)	R52(6,1), I53(9,2)
C488	N103(6,3) (*CDR3*)	
Y489		R52(9,1), S54(3,1)
Q493	S107(8,3), S108(2,2) (*CDR3*)	Y35(1,1), R52(3,4), S107(4,1), V109(7,3), R110 (4,1), G111(3,1)
S494		V109(4,2), R110(3,1), G111(4,1)
Y495		R110(10,2)
G496		R110(8,2)
Q498		R110(12,5)
N501		R110(16,4)
Y505		R110(13,4), G111(2,1), Q112(8,3)

Table 4. Characterizing the basins along the unbinding path way of hACE2 from the SARS-COV-2 S/RBD.

Residues participating in the hydrogen bond interactions				
SARS-COV-2 S/RBD	**hACE2**			
	Basin 1	**Basin 2**	**Basin 3**	**Basin4**
R403	E37(2 [b]), H34(1)	D38(4), E35(1)		
K417	D30(2)	D30(1), H34(3)	E35(2)	
G446	Q42(1)			
Y449	D38(2), Q42(1)			
Y453		E35(2)		
A475	Q24(1), S19(2)	Q24(1)		
G476	Q24(1), S19(2)			
S477	Q24(3), S19(1)	Q24(4)		
N487	Q24(3), Y83(3)	Q24(1), Y83(3)		
Q493	E35(2), H34(1), K31(2)	E35(2), H34(1), K31(2)		
G496	D38(1), K353(1)	Q42(2)		
Q498	D38(2), Q42(1), K353(2)	Q42(1), L45(1)		
T500	R357(1), N330(1), D355(1), Y41(2)	L45(1)		
N501	K353(3), Y41(1)	Q42(1)		
G502	K353(1)	Y41(1)		Q42(1)
Y505	R393(2), E37(2)	D38(2), K353(1)	Q42(2)	
Total	**51**	**35**	**4**	**1**

[b] Numbers in the parentheses represent the number of potential hydrogen bonds between S/RBD and hACE2

For a detailed list of RBD/hACE2 residues engaged in vdW interactions in the binding basins, the authors can be contacted. Shading of the rows indicates the RBD-hACE2 contact regions (light green: CR1; orange: CR2; yellow: CR3). See SI, Table S2 for short-range interactions in the binding basins.

Table 5. Characterizing the basins along the unbinding path way of antibody, B38 and mutated B38 from the SARS-COV-2 S/RBD.

Residues participating in the hydrogen bond interactions					
SARS-COV-2 S/RBD	**B38**		**Mutated B38**		
	Basin 1	**Basin 2**	**Basin 1**	**Basin 2**	**Basin 3**
R403	N92(5 [b]), Y32(1) (*LCDR1*)		N92(2) (*LCDR2*)	N92(2), Q27(1), Y32(1) (*LCDR1, 2*)	
D405	D0(2)		D0(1), Y94(1) (*LCDR2*)	Q27(1)	
E406	N92(1) (*LCDR2*)				
R408	Y94(2) (*LCDR2*)		D0(2), Y94(2) (*LCDR2*)	D0(3), Q27(3), Y94(1) (*LCDR2*)	D0(5)
Q409			Y94(1) (*LCDR2*)		
T415			T57(1)	Y58(1), (*HCDR2*), Y94(2) (*LCDR2*)	Y58(1), D0(4), Y94(2) (*LCDR2*)
T415	S56(2), Y58(2) (*HCDR2*)				
G416	S56(1)				
K417	E98(1), Y33(1), Y52(1) (*HCDR2*), N92(2), Y97(1) (*LCDR2*)	Y32(1) (*LCDR1*)	E98(2), Y33(1), N92(2), Y97(1) (*LCDR2*)	Y52(1) (*HCDR2*), N92(3) (*LCDR2*)	
D420	S56(2)		S56(2)		Y94(2) (*LCDR2*)
Y421	G54(1), S53(1), Y33(1)		G54(1), G55(1), S53(1), S56(1)	S56(1)	Y94(1) (*LCDR2*)
Y449	S31(1)		S31(1)		
Y453	N92(1), Y32(1) (*LCDR1, 2*)		N92(1) (*LCDR2*)		
L455	Y33(1)		Y33(1)		
R457			S53(2)	S56(1)	
K458	S31(1) (*HCDR1*)	A99(1), S31(1), S53(1), Y33(1) (*HCDR1*)	G54(1), S30(2), S31(1), S53(1) (*HCDR1*)	G54(1), G55(1), S56(2)	G54(1), G55(1), S56(1), T57(2)
N460	G54(1)		G54(1), G55(2), S56(3)	S56(2)	Y94(1) (*LCDR2*)
Y473	S31(2), S53(1) (*HCDR1*)		S31(2), S53(1) (*HCDR1*)	G54(1), S53(2), S56(1), Y33(1)	S56(1)
Q474		N32(1), S31(1) (*HCDR1*)	S31(1) (*HCDR1*)	S53(1) (*HCDR1*)	G54(1), S56(1)
A475			N32(1), I28(1), S31(1) (*HCDR1*)	S31(1), S53(1)	G54(1), Y33(1)
G476			Q27(1)		
S477	D0(4), G26(2) (*HCDR1*)	A99(1), R97(5), N32(2), D103(2), Y100(2) (*HCDR1, 3*)	Q27(4)	S30(3), S31(3) (*HCDR1*)	S30(1), S31(3), S53(3) (*HCDR1*)
T478	D0(1)		D0(1), Q27(4)		
E484	Y100(2) (*HCDR3*)				
N487	R97(2), G26(1), (*HCDR1, 3*)	Y100(1) (*HCDR3*)	R97(2), N32(1), G26(1), I28(1) (*HCDR1, 3*)	N32(1), Q27(2), S31(3) (*HCDR1*)	
Y489	R97(2), D103(2) (*HCDR3*)		R97(1), N32(1) (*HCDR1, 3*)	S31(1) (*HCDR1*)	
F490	Y100(2) (*HCDR3*)				
Q493	A99(1), Y32(1) (*LCDR1*)		N92(3), Y32(1) (*LCDR1, 2*)		
Y495	S30(1), S31(1) (*LCDR1*)		Y32(1) (*LCDR1*)		
G496	S30(1) (*LCDR1*)		Y32(1) (*LCDR1*)		
Q498	G68(2), S30(4), S67(1) (*LCDR1*)		S30(1), S31(1) (*LCDR1*)		
T500	Q27(1), G28(1), T69(1)		S30(1), S67(1) (*LCDR1*)		
N501	Q27(1), S30(4) (*LCDR1*)		G28(1), I29(2), S30(4), Y32(1) (*LCDR1*)	S30(2) (*LCDR1*)	
G502	G28(2)		G28(1)		
V503	D0(2), Q27(1)				
G504	D0(2)		Q27(2)	Q27(1)	
Y505	N92(1), Q90(1), L91(1) (*LCDR2*)		N92(1), Q90(1), L91(1) (*LCDR2*)	N92(2), S30(1), Y32(1) (*LCDR1, 2*)	
Total	**39 (46)**	**19 (1)**	**47 (38)**	**31 (24)**	**18 (15)**

[b] Numbers in the parentheses represent the number of hydrogen bonds that S/RBD forms in the binding basins with the antibody, B38 and its mutatnt. For detailed lists of residues engaged in vdW interactions in the two systems, the authors can be contacted. Shading of the rows (light green: CR1; orange: CR2; yellow: CR3) refers to the RBD-hACE2 contact regions (*cf.* Table-4) The reported CDRs of the inhibitors are indicated. [47] Residues colored in blue and red represent those from the heavy and light chains of the antibodies, respectively. See SI, Table S2 for short-range interactions in the binding basins.

Table 6. Characterizing the basins along the unbinding pathway of nanobody Ty1 and designer Ty1-based peptide from the SARS-COV-2 S/RBD.

Residues participating in the hydrogen bond interactions						
SARS-COV-2 S/RBD	**Nanobody (Ty1)**			**(Ty1-based) Designer peptide**		
	Basin 1	**Basin 2**	**Basin 3**	**Basin 1**	**Basin 2**	**Basin 3**
R346	Q3(4), Q5(1)					
S349	Q3(4)					
Y351	V4(1)	Q112(2)				
R403				Q5(2), V4(1)		
E406				Q5(3)		
Q409				Q3(2), Q5(2)		
K417				Q5(3), G28(1), L6(1), F29(1)		
D420				S32(2), T30(1)		
Y421				F31(2)		
K444	Q112(1)					
V445	Q112(1)					
G446	Q112(1)					Q3(1), Q5(1)
G447	Q112(1)					
N448	Q112(2)					
Y449	R110(1), Q112(1)			N56(2)		R52(1), E48(2), S51(1), V50(1)
N450	Q112(4), Q3(3), Q5(3)					
Y453				Q5(1)		
K458				S33(1), V34(1)	K45(1), M36(1), Y35(1)	
S459				S32(1), S33(1)		
N460				F31(1), S32(5), S33(3)		
T470	G28(1), T30(1) (*CDR1*)	Q112(1), Q3(2), Q5(3)				
Y473				G44(1), K45(1)	G44(2)	
A475				K45(1)	S33(1), V34(1)	
G476					S33(1)	
S477					S32(4)	
G482	S33(1) (*CDR1*)		Q112(1)			
E484	N103(1), S33(1), Y35(1) (*CDR1, 3*)	S107(6) (*CDR3*)	R110(7), S107(2) (*CDR3*)	R52(3), N103(2), L102(1), L104(1), S54(2), W49(2)	R52(3), N103(1), L102(1), L104(1), S105(2), S54(2), W49(2)	N56(4)
G485	N103(1) (*CDR3*)					
F486	N103(1) (*CDR3*)		S107(1) (*CDR3*)			
N487	N103(3) (*CDR3*)			K45(2)	Q3(5), S32(3), S33(4)	
Y489				G46(1), K45(1)	Q3(2), G46(1)	
F490				R52(2)	R52(2)	
Q493	S107(3[b]), S108(2) (*CDR3*)			I53(3), S51(1)	I53(3), S51(1)	
S494				I53(2)	I53(2)	R52(1)
Y495						Q3(1)
G496						Q3(1)
Q498						Q3(6), V4(1)
T500						Q3(5)
N501						Q3(3)
Y505				Q3(2)		Q3(1)
Total	**45**	**14**	**11**	**65**	**47**	**30**

[b] Numbers in the parentheses represent the number of hydrogen bonds that the S/RBD forms with the nanobody, Ty1 and the designed peptide in the binding basins. For a detailed list of residues engaged in vdW interactions in the two systems, the authors can be contacted. Shading of the rows (light green: CR1; orange: CR2; yellow: CR3) refers to the RBD-hACE2 contact regions (*cf.* Table-4). The reported CDRs of the nanobody is indicated.[50] See SI, Table-S2 for short-range interactions in the binding basins.

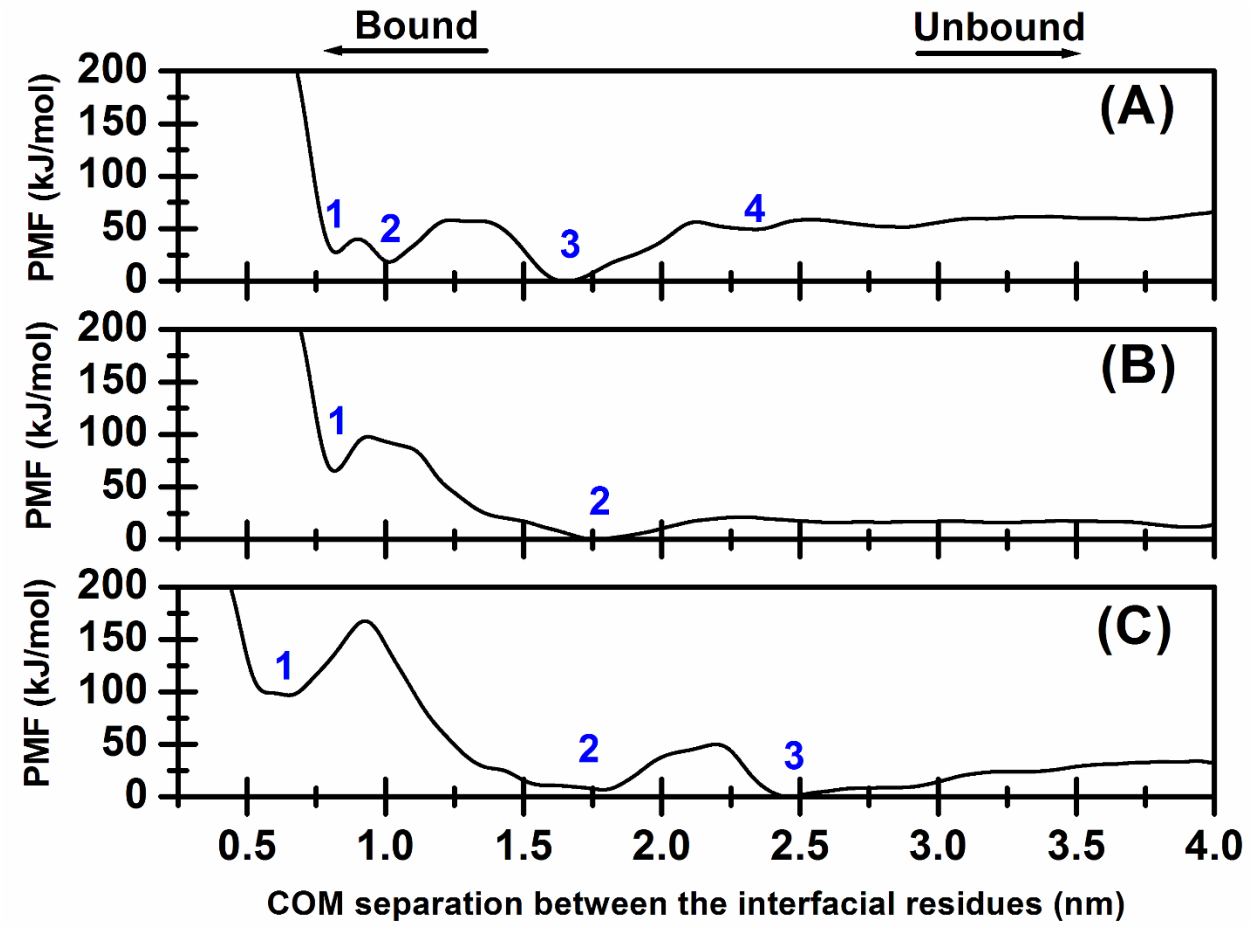

Figure 1. PMF profiles for the unbinding transitions of (A) hACE2, (B) B38, and (C) Ty1 from the SARS-COV-2 S/RBD by employing center-of-mass separation between the interfacial residues as a collective variable are shown. The PMF profile is generated from the converged well-tempered metadynamics simulations. The basins along the unbinding path are marked by blue numerals.

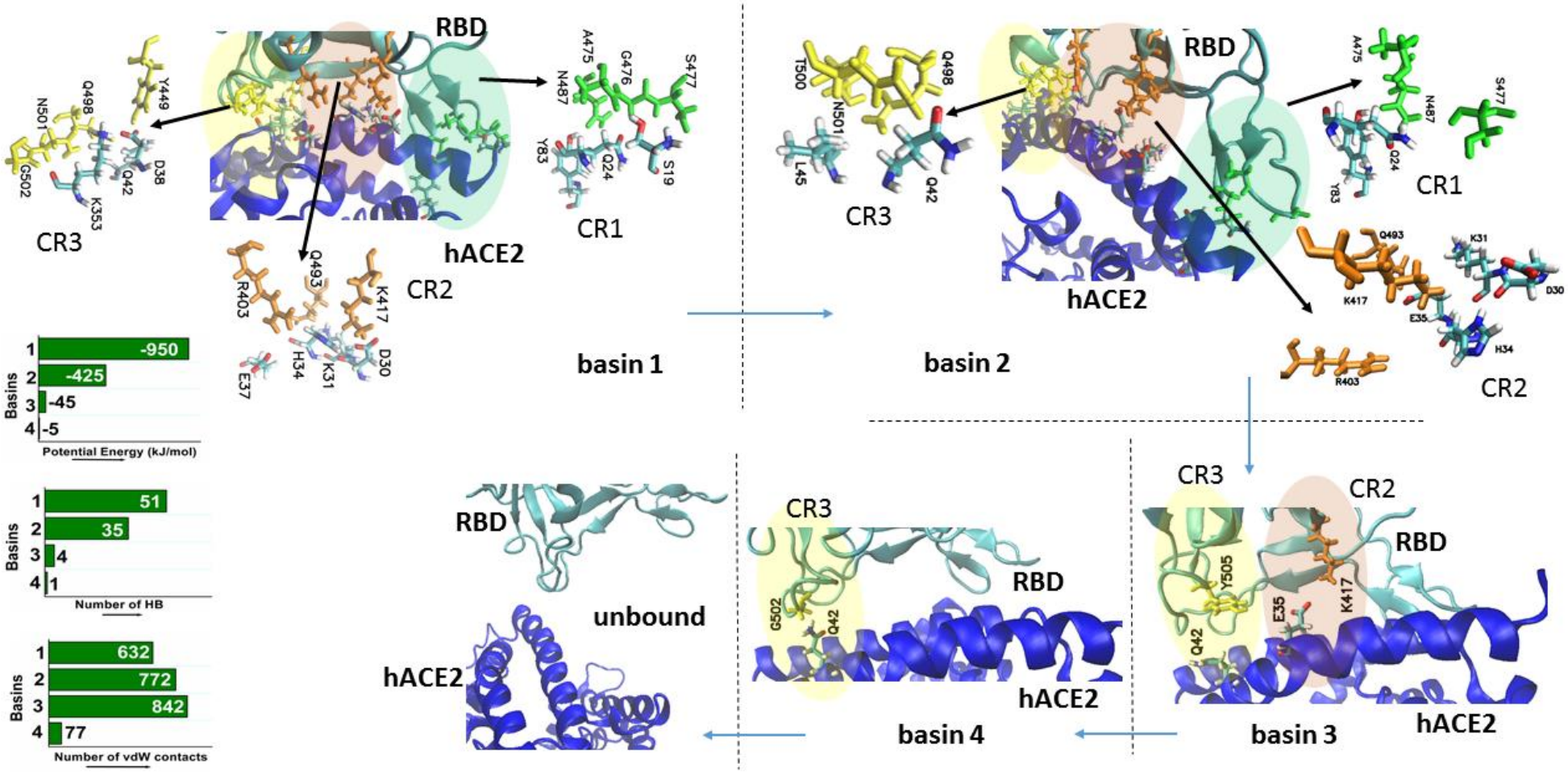

Figure 2. Snapshots of the basins (marked in Figure 1) along the unbinding pathway (until the completely unbound state) of hACE2 (blue) from the RBD of SARS-COV-2 (cyan) are shown. Only the interfacial region along with few important residues responsible for the stabilization of a particular bound state through hydrogen bond in the contact regions (CR1 to CR3) of the complex are shown The contact residues (regions) of the RBD are coloured (shaded) in green (CR1), orange (CR2) and yellow (CR3). Potential energy, number of potential hydrogen bonds, and vdw contacts between the SARS-COV-2 RBD and hACE2 in the 4 basins are shown by bar diagram. See Table-4 and SI, Table S2 for detailed characterizations of the basins.

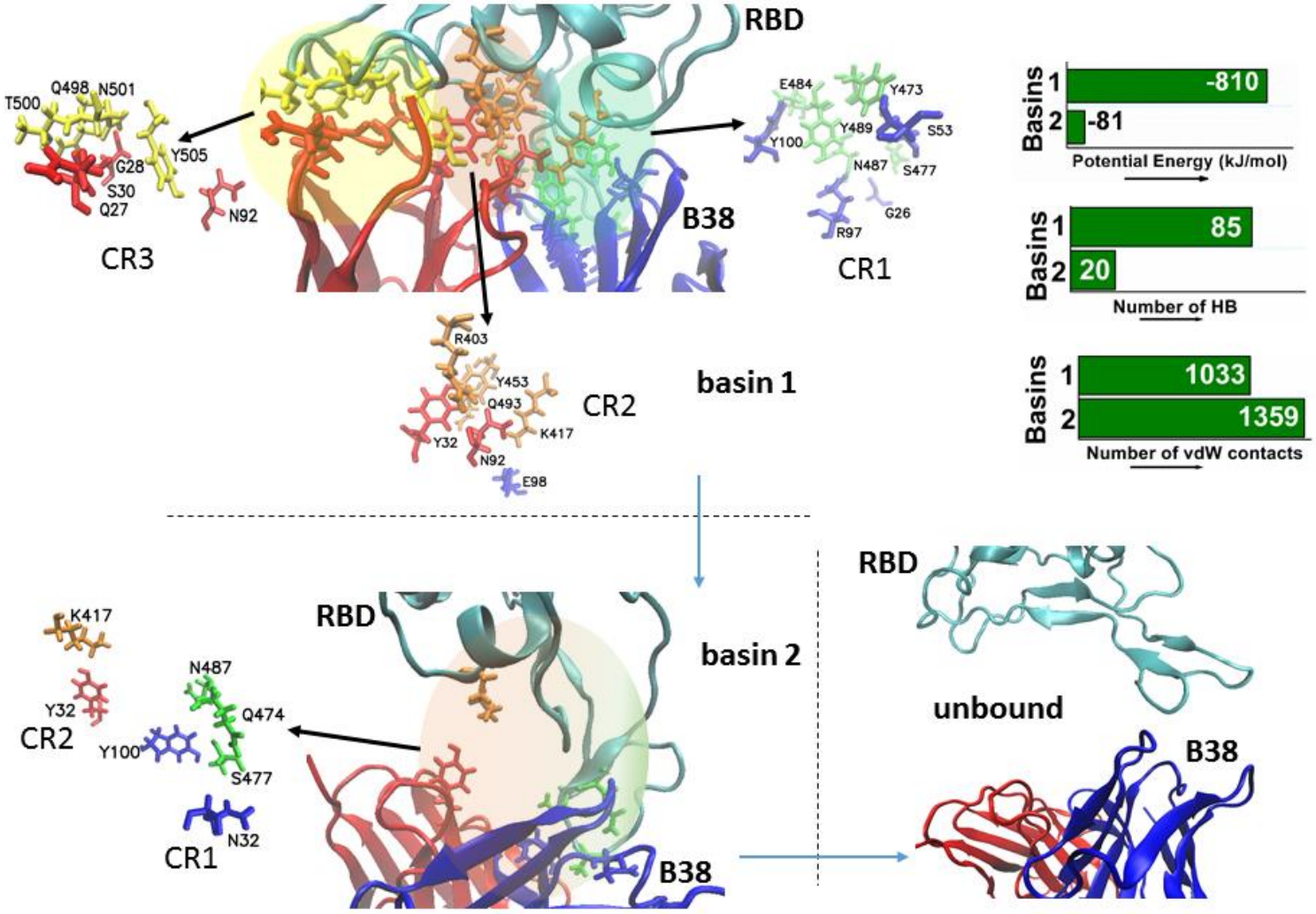

Figure 3. Snapshots of the basins (marked in Figure 1) along the unbinding pathway (until the completely unbound state) of the Fab (B38) (blue: heavy chain, red light chain) from the RBD of SARS-COV-2 (cyan) are shown. Only the interfacial region along with few important residues responsible for the stabilization of a particular bound state through hydrogen bonds are shown. The three contact regions (residues) of the RBD, prevalent in the RBD-hACE2 complex are shaded (colored) in green (CR1), orange (CR2), and yellow (CR3) for easy recognition of the epitope regions of the antigen. Potential energy, number of potential hydrogen bonds, and vdw contacts between the SARS-COV-2 RBD and the Fab in the two basins are shown by bar diagram. See Table-5 and SI, Table S2 for detailed characterizations of the basins.

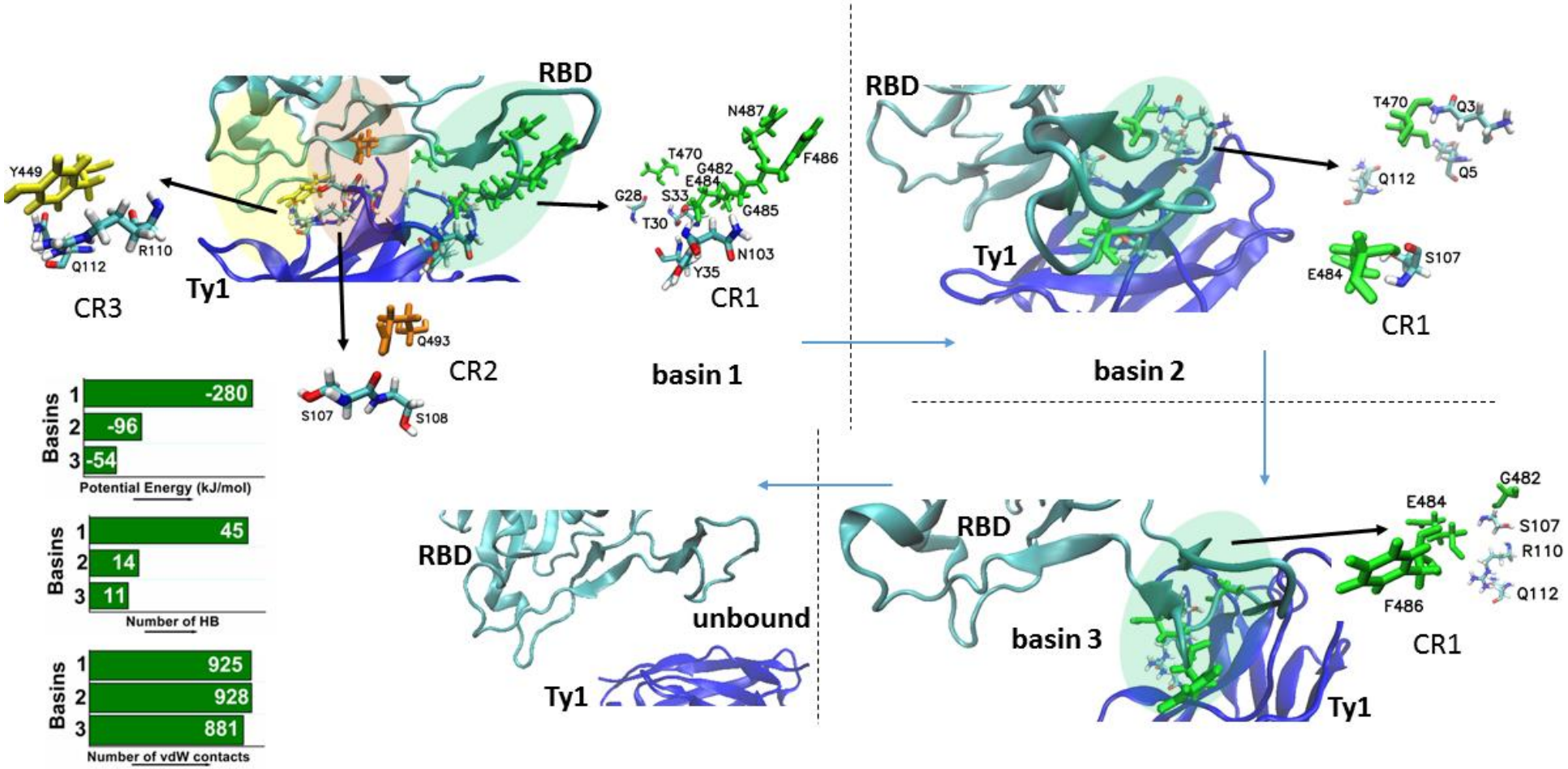

Figure 4. Same as Figure 2 but for the unbinding transition of nanobody Ty1 (blue) from the RBD of SARS-COV-2 (cyan). See Table-6 and Table S2 for detailed characterizations of the basins.

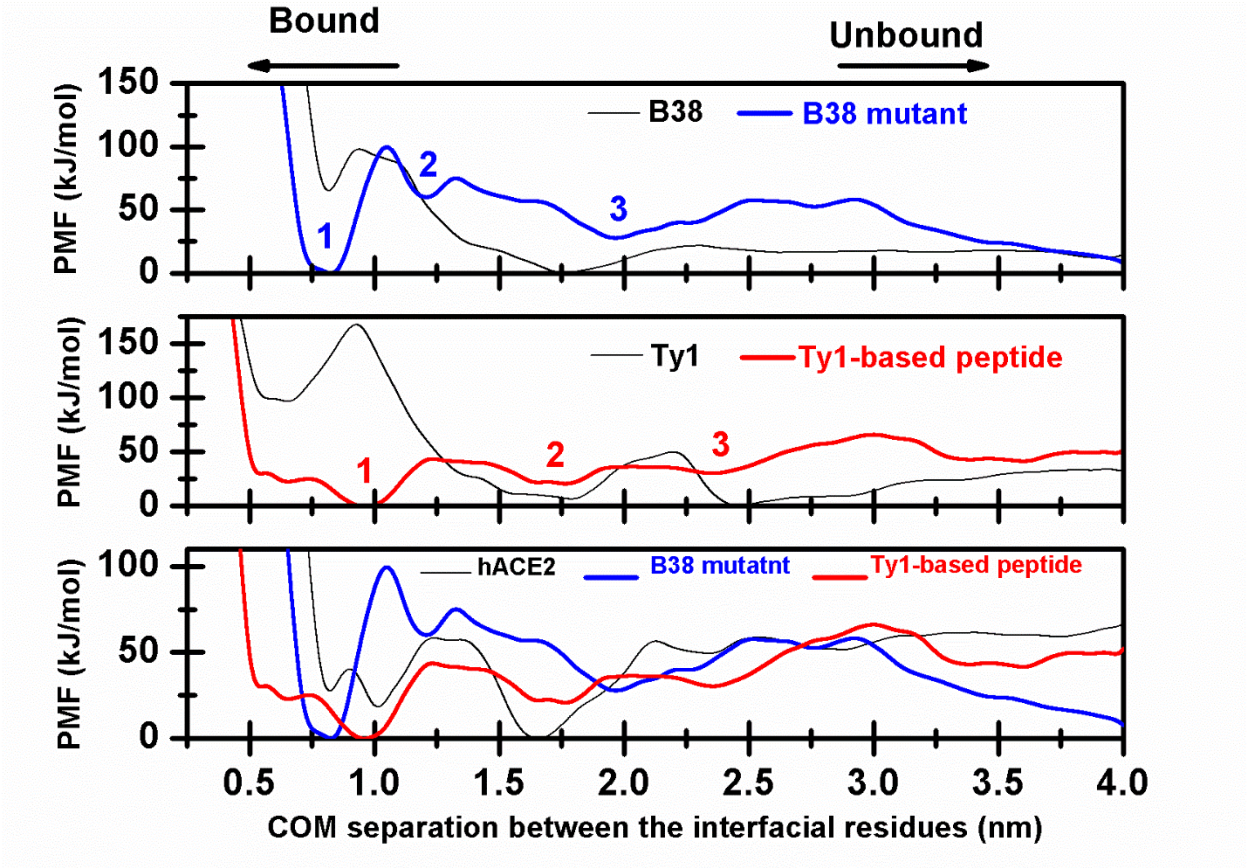

Figure 5. PMF profiles for the unbinding transitions of (upper panel) mutated B38 and (middle panel) Ty1 based designer peptide from the SARS-COV-2 RBD by employing center-of-mass separation between the interfacial residues as a collective variable are shown. The PMF profile is generated from the converged well-tempered metadynamics simulations. The basins along the unbinding path are marked by numerals. Also shown in these panels are the unbinding profiles of wild B38 and Ty1 (black lines) for the sake of comparison (see Figure 1). The bottom panel compares the unbinding profiles for hACE2 (see Figure 1), mutated B38, and Ty1 based designer peptide from the SARS-COV-2 RBD.

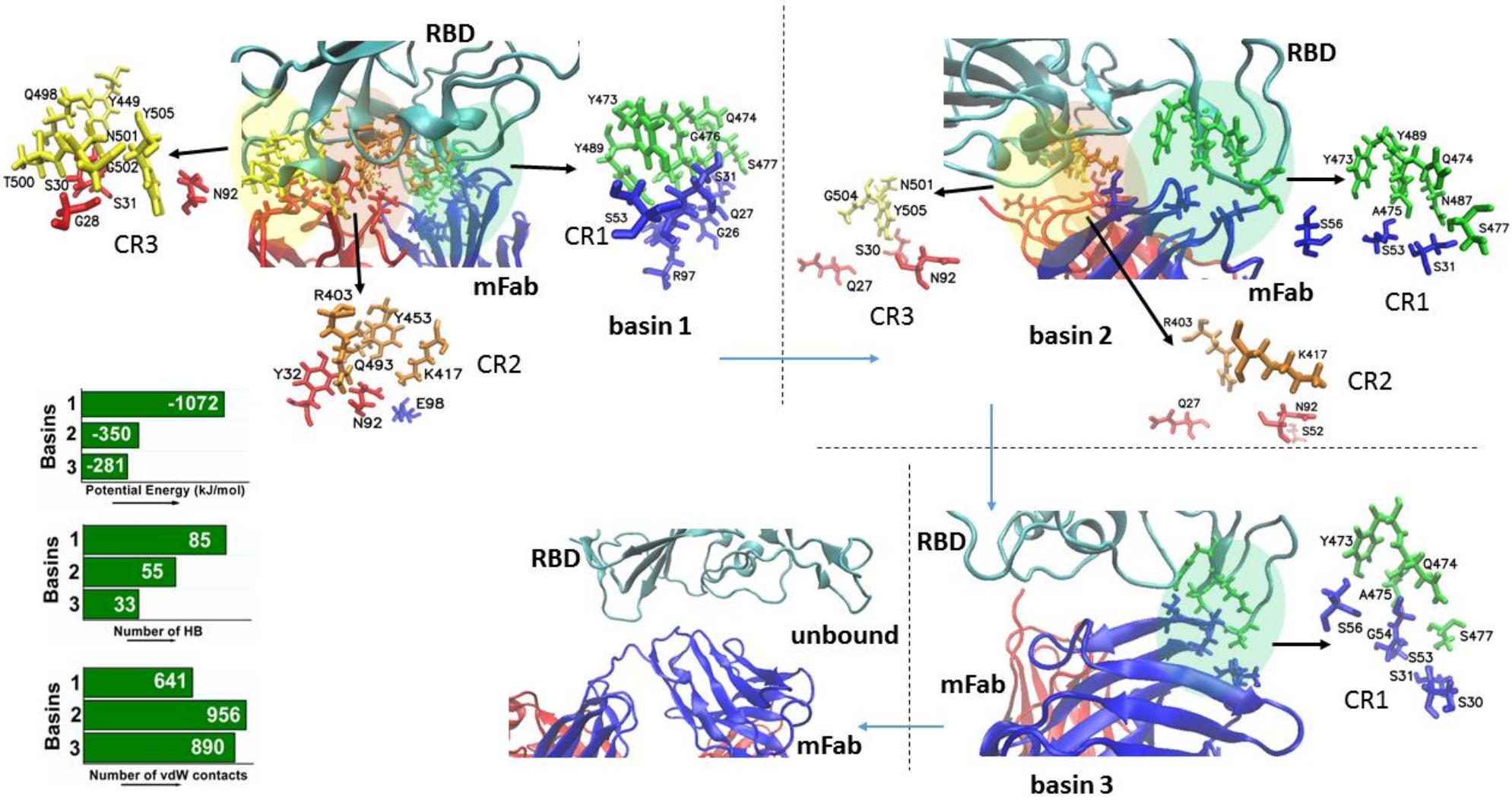

Figure 6. Same as Figure 3 but for the unbinding transition of the mFab (blue: heavy chain, red: light chain) from SARS-COV-2 RBD (cyan). See Table-5 and SI, Table S2 for detailed characterizations of the basins.

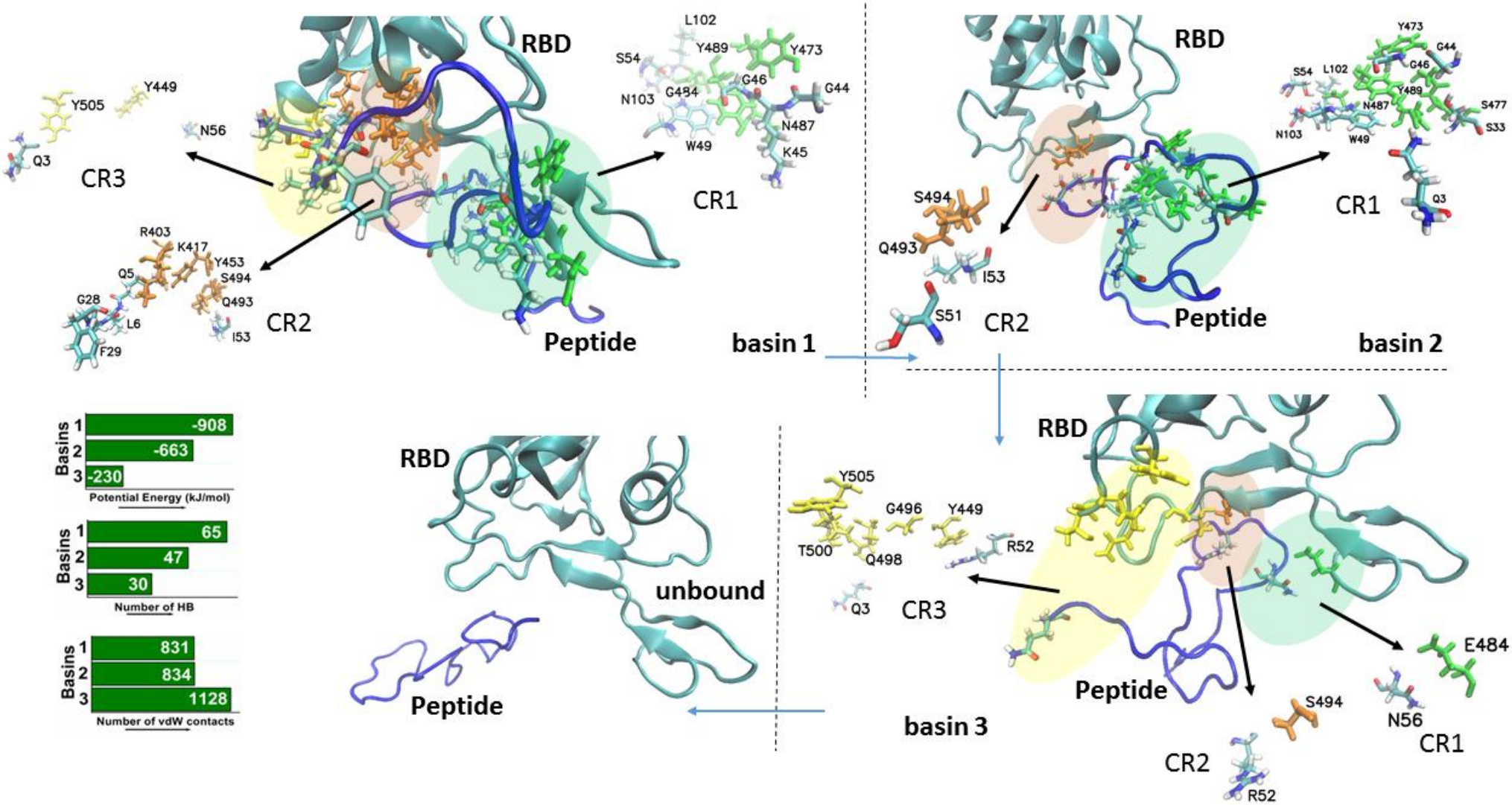

Figure 7. Same as Figure 4 but for the unbinding transition of Ty1-based designer peptide (blue) from the RBD of SARS-COV-2 (cyan). See Table-6 and SI, Table S2 for detailed characterizations of the basins.

TOC-Graphic

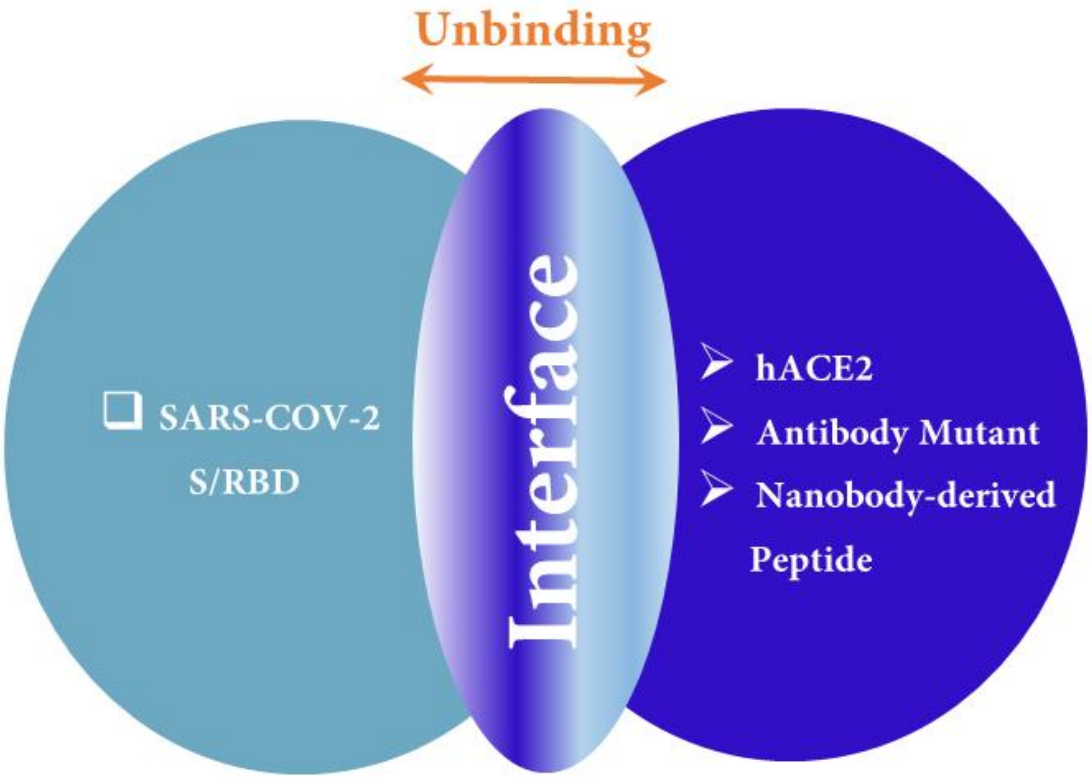
Unbinding
SARS-COV-2
S/RBD
Interface
hACE2
Antibody Mutant
Nanobody-derived
Peptide

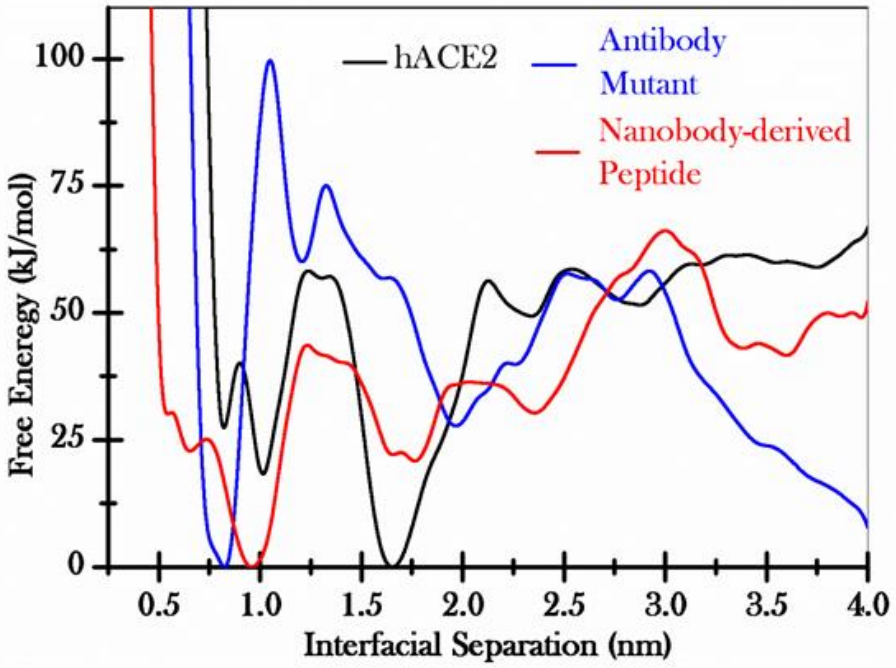
hACE2
Antibody
Mutant
Nanobody-derived
Peptide
Free Energy (kJ/mol)
100
75
50
25
0
0.5
1.0
1.5
2.0
2.5
3.0
3.5
4.0
Interfacial Separation (nm)